

A FIREBALL AND POTENTIALLY HAZARDOUS BINARY NEAR-EARTH ASTEROID (164121) 2003 YT₁

TOSHIHIRO KASUGA,^{1,2} MIKIYA SATO,³ MASAYOSHI UEDA,³ YASUNORI FUJIWARA,³ CHIE TSUCHIYA,¹
 AND JUN-ICHI WATANABE¹

¹*National Astronomical Observatory of Japan, 2-21-1 Osawa, Mitaka, Tokyo 181-8588, Japan*

²*Department of Physics, Faculty of Science, Kyoto Sangyo University, Motoyama, Kamigamo, Kita-ku, Kyoto 603-8555, Japan*

³*The Nippon Meteor Society, Japan*

(Accepted on Oct 13, 2019. The Astronomical Journal, in press)

ABSTRACT

We present a fireball detected in the night sky over Kyoto, Japan on UT 2017 April 28 at 15^h 58^m 19^s by the SonotaCo Network. The absolute visual magnitude is $M_v = -4.10 \pm 0.42$ mag. Luminous light curves obtain a meteoroid mass $m = 29 \pm 1$ g, corresponding to the size $a_s = 2.7 \pm 0.1$ cm. Orbital similarity assessed by D-criterions (cf. $D_{SH} = 0.0079$) has identified a likely parent, the binary near-Earth asteroid (164121) 2003 YT₁. The suggested binary formation process is a YORP-driven rotational disintegration (Pravec & Harris 2007). The asynchronous state indicates the age of $< 10^4$ yr, near or shorter than the upper limit to meteoroid stream lifetime. We examine potential dust production mechanisms for the asteroid, including rotational instability, resurfacing, impact, photoionization, radiation pressure sweeping, thermal fracture and sublimation of ice. We find some of them capable of producing the meteoroid-scale particles. Rotational instability is presumed to cause mass shedding, in consideration of the recent precedents (e.g. asteroid (6478) Gault), possibly releasing mm-cm scale dust particles. Impacts by micrometeorites with size $\simeq 1$ mm could be a trigger for ejecting the cm-sized particles. Radiation pressure can sweep out the mm-sized dust particles, while not sufficient for the cm-sized. For the other mechanisms, unprovable or unidentified. The feasibility in the parental aspect of 2003 YT₁ is somewhat reconciled with the fireball observation, yielding an insight into how we approach potentially hazardous objects.

Keywords: Solar system — Meteoroids, Micrometeoroids, Meteors, Fireballs, Meteor radiants — Small solar system bodies, Asteroids: individual ((164121) 2003 YT₁), Near-Earth objects — Surveys — Catalogs

1. INTRODUCTION

The worldwide meteor survey networks have established the procedure for identifying meteoroid orbits in streams and associated parent bodies, asteroids and comets, mostly known as near-Earth objects (NEOs) (SonotaCo 2009; Rudawska & Jenniskens 2014; Ye et al. 2016; Jenniskens 2017). Some NEOs, meteorite falls and fireballs have been linked with potentially hazardous asteroids (PHAs) (Madiedo et al. 2013, 2014; Svetsov et al. 2019) of which the Taurids are studied in many cases (Brown et al. 2013; Olech et al. 2017; Spurný et al. 2017; Clark et al. 2019). Physical disintegration of NEOs result in producing orbit-hugging dust (streams) which may cross the Earth orbit. Suggested mechanisms, especially for those of asteroids, include rotational instability, thermal stress, collisions (impacts) and so on (Jewitt 2012; Jewitt et al. 2015). Asteroidal stream parents should be, or used to be losing mass, while among the few mass-loss activities other than activity driven by sublimation of ice are identified (Kasuga & Jewitt 2019).

A relatively slow, bright fireball was detected in the sky over Kyoto, Japan on UT 2017 April 28 at 15^h 58^m 19^s through the SonotaCo Network (SonotaCo 2009). The small semimajor axis ($a=1.111$ AU) and high inclination ($i = 43.9^\circ$) present its peculiar orbit. The dynamical properties, as given by orbit-linking D -criterions (cf. Southworth & Hawkins 1963), find a close association with the near-Earth asteroid (NEA) (164121) 2003 YT₁ (hereafter, 2003 YT₁) (See details in Section 3). The short distance from the asteroid orbit to the Earth orbit (cf. 0.0026 AU at the descending node) is compatible with those of meteoroid streams for showers ($\lesssim 0.01$ AU, Vaubaillon et al. 2019), suggesting that both the fireball and 2003 YT₁ practically cross the Earth orbit. This asteroid-meteor pair is likely to be secured, giving a rare opportunity for understanding of meteoroid production.

The NEA 2003 YT₁ was discovered on UT 2003 December 18 in the course of the Catalina Sky Survey (Tichy et al. 2003). Based upon the absolute magnitude $H=16.2$ and the low Minimum Orbit Intersection Distance (MOID) ~ 0.003 AU (NASA/JPL Small-Body Database), the object is a PHA (Larson et al. 2004; Hicks et al. 2009). The impact probability to the Earth is calculated $\sim 6\%$ per 10^7 yr (Galiazzo et al. 2017). The Arecibo radar delay-Doppler and optical photometric observations independently identified 2003 YT₁ has a binary system (Nolan et al. 2004a). Suggested formation process is a rotational instability, a breakup/fission driven by Yarkovsky-O'Keefe-Radzievskii-Paddack (YORP) torques (Pravec & Harris 2007). The primary has 1.1 ± 0.2 km in diameter (D_p) and the secondary with a diameter of 0.21 ± 0.06 km (D_s), having a distance of 2.7 km (Nolan et al. 2004b). The primary's rotation period is 2.343 ± 0.001 hr, and the light curve amplitude of ~ 0.16 mag exhibits its nearly spheroidal shape (Galád et al. 2004; Larson et al. 2004; Warner et al. 2018). The secondary's rotation period $\lesssim 6$ hr and its orbital period of ~ 30 hr (eccentric orbit) suggest the asynchronous state (Nolan et al. 2004a,b). Geometric albedos (in visual and infrared) are measured by thermal infrared observations, $p_v = 0.24 \pm 0.16$ from the ground-based (Delbo et al. 2011), and $p_v = 0.20 \pm 0.10$ and $p_{IR} = 0.33 \pm 0.14$ from the space (WISE/NEOWISE, Mainzer et al. 2012). Near-infrared spectra (0.7–2.5 μ m) reveal the surface assemblage dominated by orthopyroxene with any lack of olivine content on 2003 YT₁, implying taxonomically V-type asteroid (Abell et al. 2004, 2005; Sanchez et al. 2013). The regolith breccia (< 25 μ m in size mostly, Ieva et al. 2016) could be originated in a larger, extensive-igneous processed precursor body (HED: howardites, eucrites, and diogenites-assemblage). The V-type NEAs (Cruikshank et al. 1991) remain an open question for their origin (from (4) Vesta?) (Cochran et al. 2004; Burbine et al. 2009).

In this paper we present the orbital and physical properties of Kyoto fireball taken by SonotaCo Network, including the trajectory, radiant point, geocentric velocity, orbit and meteoroid mass (size) and further discuss the possible relation to the parental binary NEA 2003 YT₁ by examining its potential dust production mechanisms.

2. SONOTACO NETWORK

The fireball studied here is from the SonotaCo Network database. Automated multi-station video observations use more than 100 cameras at 27 sites in Japan (SonotaCo 2009)¹. The database is advantaged in the similar type of camera setup of all the network sites. The CCD cameras are mostly WATEC series with $f=3.8\text{--}12\text{ mm}$ lens having field of view (FOV) $\approx 30^\circ - 90^\circ$. The video format is digitized in 720×480 or 640×480 pixels AVI from the NTSC signal (29.97 frames per second, interlaced), and the video field with time resolution of $\simeq 0.017\text{ sec}$ ($1/59.94\text{ sec}$) is used for measurement. Meteors are detected by UFOCaptureHD2 software, and the data reductions and orbit determinations are conducted by UFOAnalyzerV2 and UFOOrbitV2 respectively. Limiting magnitude for multi-station observations is estimated to be apparent magnitude $< +3$ and absolute magnitude $< +2$ for each (SonotaCo 2009).

The database includes orbital and physical parameters of meteors, such as trajectory (apparent position on the sky plane), radiant point, geocentric velocity, orbital elements, brightness (magnitude) and height above the sea level². Astrometry and photometric calibrations for meteors are conducted using field stars in the background and SKY2000 Master Catalog, Version 4 (Myers et al. 2001) installed in the UFOAnalyzerV2. Single-station observation has some uncertainties of measurements but negligibly small, as estimated by position in the sky plane $\sim 0.03^\circ$ (SonotaCo 2009), distance to meteor $\lesssim 200\text{ m}$ and elevation angle $\sim 0.02^\circ\text{--}0.03^\circ$. Lens distortion is corrected by background stars' positions fitted by polynomial equation. The aperture radius used for the stars is 5pix in the image ($\sim 0.5^\circ$) and the sky background is determined within a concentric annulus having projected inner and outer radii of 5pix and 7.5pix ($\approx 0.5^\circ\text{--}0.7^\circ$), respectively. For meteors on the other hand, the aperture sets a minimum rectangle that covers the total brightness of meteor including its tail, and the sky background was subtracted by the field prior to the meteor appearance. More than 5 background stars are used to count the flux of meteor. Then we obtain apparent magnitude of meteor, $m(\text{obs})$. The photometric uncertainty (mag) is estimated from typical uncertainty of comparison stars $\sim 0.5\text{ mag}$ and correction for saturated apparent magnitude of meteor, expressed as

$$\sqrt{0.5^2 + (m(\text{obs})' - m(\text{obs}))^2}, \quad (1)$$

where $m(\text{obs})'$ is corrected apparent magnitude. The $m(\text{obs})'$ is derived from $m(\text{obs})' = m(\text{obs}) + k(m(\text{obs}))^2$, where $m(\text{obs}) < 0$ and $k = -0.03$. Details of the analysis procedure is described in the UFOAnalyzerV2 manual³, and private communication with SonotaCo.

3. RESULTS

Fireball trajectory and observing sites (ID⁴) are shown in Figure 1. The images of fireball are represented in Figure 2. This event was simultaneously detected at eleven sites with twelve cameras.

¹As of 2018, <http://sonotaco.jp/doc/SNM/2018A.txt>

²<http://sonotaco.jp/doc/SNM/index.html>

³http://sonotaco.com/soft/download/UA2Manual_EN.pdf

⁴Here we note in the ID that is a assignment for observing site. Take TK8_S7 (Tokyo data) for example, the location is expressed as TK8 and the underscore S7 is named after camera.

The data sets taken at Tokyo (TK8_S7) and Osaka (Osaka03_3N) have imaged the most part of trajectory, from the beginning to the end. Numbers of video fields which have acquired the fireball position and brightness are 159 out of 173 in the Tokyo data and 194 out of 204 in the Osaka data respectively. Therefore these two data sets are primarily used for orbit determinations and photometric measurements. Orbital results are listed in Tables 1, 2, and 3. Photometric results are given in Tables 4 and 5.

3.1. *D-criterions*

We searched dynamical similarities between the fireball and asteroids using distances defined in the orbital elements space, *D*-criterions, by comparing a (semimajor axis), e (eccentricity), i (inclination), q (perihelion distance), ω (argument of perihelion) and Ω (longitude of ascending node) (Williams et al. 2019). Three types of *D*-criterions are used to reduce biases therein. The first one is D_{SH} (Southworth & Hawkins 1963) depending mostly on q , the second is D' (Drummond 1981) depending mostly on e , and the third is D_{ACS} (Asher et al. 1993) neutralizing rapid evolutions of the ω and Ω with time (cf. Dumitru et al. 2017). A smaller D indicates closer degree of orbital similarity between two bodies. By comparing with the orbit of 2003 YT₁ (see Table 3), we find more than one order of magnitude smaller values than the significant empirical threshold (e.g. $D_{\text{SH}} \lesssim 0.10\text{--}0.20$, Williams et al. 2019). The close-knit orbit interprets that 2003 YT₁ is a possible parent body. Results are shown in Table 6.

We further searched other probable meteors having the similar orbits from the SonotaCo data sets in 2007–2018 and the European video Meteor Network Database (EDMOND⁵) (Kornoš et al. 2014a,b) in 2001–2016, but found few compelling cases (Appendix A).

3.2. *Meteoroid Mass*

For initial meteoroid mass, the classical meteor luminous model (Bronshten 1983; Ceplecha et al. 1998) has been used but with non-negligible uncertainty in ablation coefficient. Instead, we have made a new meteor luminous model as described in the Appendix B.

The total mass of meteoroid (source of fireball), m (g), can be estimated from the light curves (Figure 3) using the new luminous model (Equation (B9)), given by

$$m = \sum_N \left[\frac{2I}{\tau v^2} \left(\frac{2}{\sigma v^2} - 1 \right)^{-1} \int_0^t dt \right]_N, \quad (2)$$

where N is the number sign of video field (see Tables 4 and 5), I is the meteor luminosity, τ is the luminous efficiency, v is the meteor velocity (cm s^{-1}), σ is the ablation coefficient ($\text{s}^2 \text{km}^{-2}$) and t is the time (s). We define the meteor luminosity in visual magnitude-based units as $I = 10^{-0.4M_v}$, where M_v is the absolute magnitude (as seen from distance of 100 km).

The luminous efficiency, τ , is the fraction of a meteoroid's instantaneous kinetic energy loss converted into light in a particular band-pass. The uncertainty within is substantial (0.05~10 s %) as it depends on many factors, e.g. the speed, mass, composition of meteoroid and the height at which it ablates (different flow regimes) and spectral sensitivity of detector (cf. Weryk & Brown 2013; Subasinghe & Campbell-Brown 2018) (See the review, Popova et al. 2019). For this study, we use the

⁵<http://www.daa.fmph.uniba.sk/edmond>

velocity dependence (Table 1 in Ceplecha & McCrosky 1976) considering the performance of CCD cameras (e.g. low resolution). Setting $v=23.7\text{ km s}^{-1}$ finds $\tau=5\times10^{-13}\text{ erg}^{-1}\text{ s}^0\text{mag}$. The τ -value corresponds to 0.75% efficiency. The conversion is given by multiplying $1.5\times10^{10}\text{ erg s}^{-1}\text{ 0mag}^{-1}$, i.e. the luminous energy equivalent to zero magnitude in visual (Table VI in Ceplecha et al. 1998).

The critical bulk density, ρ , for the meteoroid and 2003 YT₁ is estimated. An asteroid shape is approximated as an ellipsoid with axes $a \geq b = c$, in rotation about the c-axis. A limit to the ratio of the equatorial axes is, $f=a/b=10^{0.4\Delta m}$, where Δm is the light curve amplitude. Rotation around the c-axis with period, P_{rot} , gives a condition that the gravitational acceleration is greater than the centripetal acceleration which is the largest at the top of the shape. The net acceleration toward the center of a rotating object is > 0 , giving the relation as (Equation (4) of Jewitt & Li 2010),

$$\rho > \left(\frac{3\pi}{GP_{\text{rot}}^2} \right) \left(\frac{a}{b} \right)^2, \quad (3)$$

where G is the gravitational constant. We substitute $G = 6.67 \times 10^{-11}\text{ m}^3\text{ kg}^{-1}\text{ s}^{-2}$, $P_{\text{rot}} = 2.343\text{ hr}$, $\Delta m = 0.16\text{ mag}$ (i.e. $f=a/b=1.16$) into Equation (3), then obtain $\rho \gtrsim 2700\text{ kg m}^{-3}$. This is consistent with the lower limit for rubble pile asteroids with diameters of 0.3–10 km ($\rho = 2.7\text{ g cm}^{-3}$), as formulated by the observed light curve amplitude versus spin rate (Pravec 2005). The proposed bulk density $2010 \pm 700\text{ kg m}^{-3}$ (Brooks 2006) may be uncertain due to the assumption of circular orbit of the secondary. The orbit is actually eccentric ($e \simeq 0.18$, Fang & Margot 2012) (cf. Pravec et al. 2016).

Substituting $v(=v_g)=2.37\times10^6\text{ cm s}^{-1}$, $\tau=0.75\%$, $\sigma = 0.0017\text{ s}^2\text{ km}^{-2}$ (Appendix B) and $t = 0.017\text{ s}$ into Equation (2), we obtain m (see Tables 4 and 5). The weighted mean of total mass is $m=29\pm1\text{ g}$, corresponding to meteoroid size $a_s=2.7\pm0.1\text{ cm}$ for $\rho = 2700\text{ kg m}^{-3}$. For reference, the classical luminous model (Equation (B2)) is applied too. The resulting masses are compared in Table 7.

4. DISCUSSION

Here, we recapitulate the binary formation process of 2003 YT₁ and evaluate possible dust production mechanisms for mm-cm scale particles.

4.1. Binary Formation

The 2003 YT₁ binary system is presumed to be formed from a breakup/fission by rotational instability with YORP spin-up. The primary with $D_p \lesssim 10\text{ km}$ and the normalized total angular momentum of the binary system α_L ⁶ = 1.13 suggest that the 2003 YT₁ binary system was formed from a precursor body spinning at the critical rate, resulting in fission and mass shedding (Group A in Table 1 and Figures 2 and 3 from Pravec & Harris 2007) (Reviewed in Margot et al. 2015; Walsh & Jacobson 2015). The 2003 YT₁ primary rotates ($P_{\text{rot}}=2.343\text{ hr}$) closely to the spin barrier period $\sim 2.2\text{ hr}$ (Warner et al. 2009; Chang et al. 2015). This can reasonably lead to a rotational breakup when centrifugal forces have exceeded the gravitational and cohesive forces (Pravec et al. 2008).

⁶The α_L is the ratio of the total angular momentum of the system to the angular momentum of a critically spinning spherical body. The spherical body is comprised of the mass and volume equivalent to the two objects of the binary system. The internal friction angle is 90° (Pravec & Harris 2007).

We calculate the YORP timescale of the spin, τ_Y , using the ratio of the rotational angular momentum, L , to the torque, T . The relation is given by Jewitt et al. (2015) as,

$$\tau_Y \sim K D_e^2 R_h^2, \quad (4)$$

where K is a constant, D_e is the asteroid diameter (km) and R_h is the heliocentric distance (AU). The value of constant K is experimentally estimated from published measurements of YORP acceleration in seven well-characterized asteroids (Table 2 from Rozitis & Green 2013). Scaling K to the bulk density of primary $\rho = 2700 \text{ kg m}^{-3}$ and its rotation period $P_{\text{rot}}=2.343 \text{ hr}$, we find $K \sim 5 \times 10^{13} \text{ s km}^{-2} \text{ AU}^{-2}$. By Equation (4), the primary with $D_e (=D_p)=1.1 \text{ km}$ orbiting at $R_h \sim 1.11 \text{ AU}$ takes $\tau_Y \sim 2 \text{ Myr}$. This is consistent with the previous study ($\sim 1 \text{ Myr}$, Vokrouhlický et al. 2015) and much shorter than the catastrophic collisional lifetime for 1-km NEAs ($\sim 100 \text{ Myr}$, Bottke et al. 1994) (see also Section 4.2.3). The YORP spin-up plays a contributory role.

The cohesive strength is a required parameter for asteroids rotating near or faster than the spin-barrier to resist rotational forces (Scheeres et al. 2010). The strength at a rotational breakup of a body is estimated by $S_c \sim \rho (D_s/D_p) (\Delta v)^2$ (Equation (5) of Jewitt et al. 2015), where D_p and D_s are the dispersed fragmental sizes of primary and secondary respectively, Δv is the excess velocity of escaping fragments, assumed comparable to the escape velocity (v_e) from the primary, and ρ is the bulk density. With the same value for ρ (see section 3.2) and substituting $(D_s/D_p) = 0.19$ (the diameter ratio of the secondary to primary), and $\Delta v (=v_e) = 0.68 \text{ m s}^{-1}$, we find $S_c \sim 240 \text{ N m}^{-2}$. This value is comparable to weak, van der Waals forces ($\sim 10\text{--}100 \text{ N m}^{-2}$) bounded in a modeled rubble-pile asteroid (Scheeres & Sánchez 2018), while $10^5 \times$ weaker than those of competent rocks ($10^7\text{--}10^8 \text{ N m}^{-2}$). Therefore, given a rubble-pile structure, a rotational breakup/fission is a probable process for the 2003 YT₁ binary formation.

The breakup/fission period is inferred from the spin asynchronous state of 2003 YT₁ binary system in the present day. The timescale from asynchronous to synchronous state, τ_{sync} , limits to the age of the binary system. Two models are applied for 2003 YT₁ using the data of known synchronous binary (Table 3 in Fang & Margot 2012). One estimates $\tau_{\text{sync}}=10^{7\text{--}8} \text{ yr}$ by the tidal Love number proportional to the radius (Goldreich & Sari 2009), another estimates $\tau_{\text{sync}}=10^{4\text{--}5} \text{ yr}$ by the tidal Love number inversely proportional to the radius (Jacobson & Scheeres 2011). The former just agrees with the large-sized binaries having primary with $D_e \sim 4 \text{ km}$, on the other hand, the latter fits well for smaller-sized objects too (down to $D_e \sim 0.4 \text{ km}$). For 2003 YT₁ we thus take $\tau_{\text{sync}}=10^{4\text{--}5} \text{ yr}$ (Fang & Margot 2012). The interpretation is that this binary is age of $< 10^4 \text{ yr}$, comparable with the upper limit to meteoroid stream lifetime $< 10^4 \text{ yr}$ (Jenniskens & Lyytinen 2005).

Another example is proposed by the small-sized V-type NEA pair ($D_e \sim 25\text{--}50 \text{ m}$) also having the young age of separation $< 10^4 \text{ yr}$ ($D'=0.0035$ for 2017 SN₁₆ and 2018 RY₇) (Moskovitz et al. 2019). The YORP-driven breakups for the (sub)km-sized bodies may suggest moderately recent events.

4.2. Dust Production Mechanisms

We look into possible dust production mechanisms from 2003 YT₁. The consequences of YORP-driven breakups are reported from the (sub)km-sized main-belt asteroids, as exemplified by P/2010 A2 (Jewitt et al. 2010, 2013; Agarwal et al. 2013), P/2013 R3 (Jewitt et al. 2014a, 2017; Hirabayashi et al. 2014) and (6478) Gault (Ye et al. 2019; Moreno et al. 2019; Kleyna et al. 2019; Jewitt et al. 2019b; Chandler et al. 2019; Hui et al. 2019). Additionally, other different mechanisms

may work together, e.g. impact for P/2010 A2 and outgassing torques from sublimated ice for P/2013 R3 (Jewitt et al. 2015). Here, we estimate breakup/fission (rotational instability), resurfacing, impact, thermal fracture, photoionization, radiation pressure sweeping and sublimation of water ice.

4.2.1. Breakup/Fission (Rotational Instability)

Binary NEAs show a trend to have the large values of thermal inertia $\Gamma \gtrsim 400 \text{ J m}^{-2} \text{s}^{-0.5} \text{ K}^{-1}$, typically twice those of non-binary NEAs, suggesting the fine regoliths were swept away during the YORP-induced binary formation (Walsh et al. 2008; Delbo et al. 2011). For 2003 YT₁, it would be difficult to determine the sizes and speeds of released dust particles at the presumed breakup time, whereas the measured values of the recent precedents infer the large particles (mm–cm scale) with nearly the gravitational escape speeds $\lesssim 1 \text{ m s}^{-1}$ (cf. $a_s = 6 \text{ mm}–40 \text{ cm}$ from P/2010 A2, $\sim 1 \text{ cm}$ from P/2013 R3 and $\lesssim 1 \text{ cm}$ from Gault, Jewitt et al. 2013, 2014a, 2019b). On the process, resurfacing could be partly involved (Gault, Marsset et al. 2019). The similar situation might be expected for 2003 YT₁. The dust particles are, if released, supposed to reach the Earth within the typical stream lifetime (10^4 yr). The short distance to the Earth orbit, e.g. $\Delta r = 0.0026–0.0279 \text{ AU}$ (Table 2), may help. Accordingly, the rotational breakup/fission ejecting the mm–cm scale dust particles is considered as a likely cause.

4.2.2. Resurfacing

Planetary encounters, space weathering and thermal processes could induce resurfacing, which might lose dust particles on the surfaces to some extent. For example, the timescale for Q-type NEAs to be refreshed into S-type (at 1 AU and $q \lesssim 0.9 \text{ AU}$) is estimated $10^{5–7} \text{ yr}$ by planetary encounters (Nesvorný et al. 2010; Binzel et al. 2010), space weathering (Graves et al. 2018) and thermal processes (Graves et al. 2019). For V-type NEAs, the aftermaths of those processes are unclear (space weathering, Pieters et al. 2012; Fulvio et al. 2016), while the timescale of resurfacing itself seems to be 10–1000 times longer than the typical stream lifetime. The resurfacing is thus unlikely to be responsible for releasing the source of meteors.

4.2.3. Impact

Impacts can cause catastrophic disruption of asteroids and/or dust production. The catastrophic disruption is defined as the impact resulting in losing a half of the target’s mass. The specific impact energy threshold is expressed as $Q_D^* = (1/2)(D_i/D_t)^3 \Delta V_{\text{NEA}}^2$, where D_i , D_t and ΔV_{NEA} are the size of the impactor and the target (an assumed precursor body) and the relative velocity among NEAs, respectively (Jutzi et al. 2010). With $Q_D^* \sim 1400 \text{ J kg}^{-1}$ for catastrophic disruptions of stone meteorites (Flynn & Durda 2004; Flynn et al. 2018), $D_t \approx D_p = 1100 \text{ m}$ (assuming the primary size occupying $> 80\%$ of the precursor body) and $\Delta V_{\text{NEA}} = 17–20 \text{ km s}^{-1}$ (Bottke et al. 1994; Jeffers et al. 2001), we find $D_i \sim 20 \text{ m}$. This catastrophic event is inferred from the interval between impacts, τ_{col} (Davis et al. 2002),

$$\tau_{\text{col}} \simeq \frac{4}{\pi(D_t + D_i)^2 P_{\text{NEA}} N_i(\geq D_i)}, \quad (5)$$

where P_{NEA} is the collision frequency per unit area in the near-Earth region ($\text{km}^{-2} \text{ yr}^{-1}$), and $N_i(\geq D_i)$ is the cumulative number of impactor larger than D_i . The NEA cumulative size distribution is measured by WISE/NEOWISE, $N_i(D_i \geq 140 \text{ m}) \simeq 13200 \times (140 \text{ m}/D_i)^{1.32}$ (Mainzer et al. 2011),

and we presumably extend the equation down to 20 m in diameters. With $D_i \sim 20$ m, $N_i (\gtrsim 20$ m) $\sim 1.7 \times 10^5$, $D_t \approx D_p = 1.1$ km (see above) and $P_{\text{NEA}} = 1.5 \times 10^{-17} \text{ km}^{-2} \text{ yr}^{-1}$ (Bottke et al. 1994), we find $\tau_{\text{col}} \gtrsim 10^{11}$ yr. This is much longer than $\tau_{\text{sync}} = 10^{4-5}$ yr (Fang & Margot 2012) and the mean dynamical lifetime of NEAs $\sim 10^6$ yr (Bottke et al. 2002; Morbidelli et al. 2002), suggesting absence of catastrophic event (cf. Section 4.1).

On the other hand, micrometeorite impacts may result in ejecting the meteoroid-sized particles. The velocity distribution for micrometeorites near the Earth, U , is $12 \sim 70 \text{ km s}^{-1}$ (cf. radar observations, Nesvorný et al. 2010; Janches et al. 2014; Carrillo-Sánchez et al. 2015). For equal target and impactor densities, the ratio of the ejecta mass, m_e , traveling faster than the escape velocity, v_e , to impactor mass, m_i is related by

$$m_e/m_i = A(v_e/U)^\alpha, \quad (6)$$

where $A \sim 0.01$, $\alpha \sim -1.5$ (Housen & Holsapple 2011). Substitution $m_e \sim 30$ g (fireball mass), $v_e = 0.68 \text{ m s}^{-1}$ and $U = 12 \sim 70 \text{ km s}^{-1}$ into Equation (6), we find that micrometeorite impactors in the size range $0.4 \text{ mm} \leq a_i \leq 1 \text{ mm}$ ($m_i = (0.1 \sim 1.3) \times 10^{-3} \text{ g}$ with $\rho = 2.7 \text{ g cm}^{-3}$) can eject the cm-sized dust particles. The perpendicular impact strength $> 10^{11} \text{ N m}^{-2}$ is estimated from the equation of impact force per unit area given by $m_i U / \delta t \times 4/\pi a_i^2$, where $\delta t = a_i/U$ is the assumed extend impact time (s). The value is by orders of stronger than the compressive strengths of stone meteorites $\sim 10^8 \text{ N m}^{-2}$ (Flynn et al. 2018), suggesting micrometeorites are certainly smashing the surface. In this case, many of unknown relevant physical parameters (e.g. impact frequency, population of micrometeorite near 2003 YT₁) prevent exact estimation, however, offers probable insight for dust production.

4.2.4. Thermal Fracture

Thermal fracture and fatigue of the asteroid surfaces can be caused by desiccation stress, with the release of dust particles (Jewitt & Li 2010). For 2003 YT₁, the peak perihelion temperature $T_q \sim 440 \text{ K}$ is about half or less of those of near-Sun asteroids (cf. Phaethon, Jewitt 2013), while the thermal stress $\lesssim 50 \text{ MPa}$ is somewhat responsible for breakdown of the rocky surfaces of most asteroids in the inner Solar System (Figure 9(b) in Molaro et al. 2015). The characteristic speeds of dust particles produced by thermal disintegration can be computed by conversion from thermal strain energy into kinetic energy of ejected dust particles. We use the required conversion efficiency, η , given by (cf. Equation (3) of Jewitt & Li 2010)

$$\eta \sim \left(\frac{v_e}{\alpha \delta T} \right)^2 \left(\frac{\rho}{Y} \right), \quad (7)$$

where, again $v_e = 0.68 \text{ m s}^{-1}$, $\alpha \sim 10^{-5} \text{ K}^{-1}$ is the characteristic thermal expansivity of rock (Lauriello 1974; Richter & Simmons 1974), $\delta T \sim 80 \text{ K}$ is the temperature variation between the q and aphelion, and $Y = (1 \sim 10) \times 10^{10} \text{ N m}^{-2}$ are Young's moduli for rock in general (Pariseau 2006). With ρ as above we find $\eta \gtrsim 2\text{--}20\%$ is needed for the velocities of ejected dust particles to surpass the escape velocity. The value of conversion efficiency is small enough for most dust particles to be launched into interplanetary space.

Note that micron-sized particles are observed from the Phaethon tails at perihelion, possibly produced by a combination of thermal fracture and radiation pressure (Jewitt et al. 2013; Hui & Li 2017). Such tiny particles are distinct from the mm-cm scale dust. Larger, mass-dominant particles could be launched, but the acquisition of more and better data for estimation is waited (Jewitt et al. 2018, 2019a). This mechanism is hence pending.

4.2.5. Photoionization

Photoionization by solar UV induces electrostatic forces to eject very small particles. For a 1 km-diameter asteroid 2003 YT₁, the critical size is estimated to be $a_e \lesssim 4 \mu\text{m}$ (Equation (12) of Jewitt et al. 2015). Therefore, mm–cm scale particles cannot be launched. We conclude this process is improbable.

4.2.6. Radiation Pressure Sweeping

Small dust particles on the surface of asteroids, if they briefly lose contact forces, can be stripped away by radiation pressure sweeping. By equating the net surface acceleration (gravitational and centripetal) with the acceleration due to radiation pressure, we estimate the critical size to be swept away, a_{rad} (μm), with Equation (6) of Jewitt & Li (2010)

$$a_{\text{rad}} \sim \frac{3g_{\odot}}{2\pi R_{\text{AU}}^2 f^{1/2} D_e} \left[\frac{G\rho}{f^2} - \frac{3\pi}{P_{\text{rot}}^2} \right]^{-1}, \quad (8)$$

where, g_{\odot} is the gravitational acceleration to the Sun at 1 AU, R_{AU} is the heliocentric distance expressed in AU, f is the limit to the axis ratio ($=a/b$) and G is the gravitational constant. We substitute $g_{\odot} = 0.006 \text{ m s}^{-2}$, $R_{\text{AU}} = 0.786$ (non-dimensional), and adopt the same values of f , G , $D_e (=D_p)$, ρ and P_{rot} (as applied so far) into Equation (8), then obtain $a_{\text{rad}} \sim 2,900 \mu\text{m} \approx 3 \text{ mm}$. The mm-sized dust particles can be swept by radiation pressure from 2003 YT₁, could be the source of meteors. Even if they arrived at the Earth, the relatively small size and slow velocity would be orders of magnitude too faint meteors $m_{\text{obs}} \sim +5 \text{ mag}$ (Table I in Lindblad 1987) for most optical surveys. By contrast, the cm-sized dust particles (source of fireballs) are unlikely to be released.

4.2.7. Sublimation of Water Ice

Sublimation of water ice may be an improbable dust production mechanism for differentiated (V-type) or thermally metamorphosed (S-type) asteroids. On the contrary, the presence of aqueously altered minerals on those of surfaces have been reported (Rivkin et al. 2015, 2018), as well as further evidences, the weakly active S-type Oort Cloud object driven by sublimation of water ice (Meech et al. 2016) and the native water inclusion in Itokawa samples (Jin & Bose 2019). Asteroid (4) Vesta's current surface texture, fracture and roughness (cm- to 10 cm-scale) could be caused by (carbonaceous) impactors (Hasegawa et al. 2003; De Sanctis et al. 2012; Russell et al. 2013, 2015). By contrast, the recent Dawn bistatic radar observation indicates subsurface volatiles (water ice) involvement processes (Palmer et al. 2017).

Can buried water ice exist and survive even in V-type asteroids? The differentiation process would occur for the most part of the body, but partially may not. The Vesta's smoother terrain area (heightened hydrogen $> 0.015\%$), on which subsurface ice might contribute to, occupy only $\gtrsim 0.01\%$ of the total surface area (Palmer et al. 2017). The extreme partiality might lead to the localized subsurface ice existence.

How deep can water ice survive in the 2003 YT₁ primary, if it were therein? Megaregolith-like materials (large, rubble, brecciated bedrock), similar structure found in Vesta (Denevi et al. 2012; Hoffmann et al. 2012), have low thermal diffusivity $\kappa \sim 10^{-7} - 10^{-8} \text{ m}^2 \text{s}^{-1}$ (Haack et al. 1990; Fu et al. 2014). The diurnal thermal skin depth (at which temperature is reduced to be a factor of $1/e$), d_s , is estimated by $\sim \sqrt{\kappa P_{\text{rot}}}$. Setting $\kappa = 10^{-7} - 10^{-8} \text{ m}^2 \text{s}^{-1}$ and $P_{\text{rot}}=2.343 \text{ hr}$ find $d_s \sim 0.9 - 3 \text{ cm}$. The black body temperature at the thermal skin depth is $\sim 120 \text{ K}$ even at perihelion, below

the sublimation temperature of water ice 150 K (Yamamoto 1985). Conceivably, water ice might be preserved in the very shallow subsurface within a few cm.

To estimate the size of ejected dust particles coupled to the outflowing gas driven by sublimation of water ice, the small source approximation (SSA) model is applied (Jewitt et al. 2014b). We assume a small patch of surface water ice on 2003 YT₁, and also assume that subsurface water ice acts in a similar way to the exposed ice. Spacecraft visits to comets find too small ice exposure on the nuclei (67P/C-G, Hu et al. 2017) to explain the measured activities driven by sublimation on which a few–10s % of surface ice coverages are presumed to replenish (Tancredi et al. 2006). Alternatively, shallow subsurface water ice is proposed to be the most of contribution (67P and Ceres, Agarwal et al. 2017; Küppers 2019). A non-rotating, spherical object is assumed for the physical essence of gas dynamics. This prevents complicated gas flows caused by inhomogeneous distribution of gas release from the non-spherical object (Fulle et al. 2015; Agarwal et al. 2016). Then, ice sublimation from an exposed (\approx subsurface) ice patch located at the subsolar point is examined. We solved energy balance equation of a completely absorbing (sub)surface ice at the subsolar point, with 2003 YT₁ located at perihelion $q=0.786$ AU. The subsolar temperature at the d_s is ~ 160 K, warm enough for water ice to sublime. The flux energy completely absorbed from the sun and energy lost from the asteroid surface by radiation and latent heat of ice sublimation are calculated. The resulting maximum specific mass loss rate is $(dm/dt)_{\text{ice}} = 8 \times 10^{-4} \text{ kg m}^{-2} \text{ s}^{-1}$ at the subsolar point (at the highest temperature 206 K of the non-rotating body). The terminal velocity in the SSA by gas drag is very small compared to the gravitational escape speed from the asteroid, but certainly assist to launch dust particles from the surface into interplanetary space. The radius of ice sublimating area (patch), r_{ice} , is related with the critical size of dust particles to be ejected, a_c , as expressed by Equation (A6) of Jewitt et al. (2014b),

$$r_{\text{ice}} > \frac{8\pi G\rho^2 D_p^2 a_c}{9C_D v_{\text{gas}}} \left(\frac{dm}{dt} \right)_{\text{ice}}^{-1}, \quad (9)$$

where $C_D \sim 1$ is a dimensionless drag coefficient which depends on the shape and nature of the grain and v_{gas} is the thermal speed of gas molecules. We set $a_c=1 \text{ mm} - 1 \text{ cm}$ using $v_{\text{gas}}=490 \text{ m s}^{-1}$ (Equation (10) of Graykowski & Jewitt 2019) and $(dm/dt)_{\text{ice}} = 8 \times 10^{-4} \text{ kg m}^{-2} \text{ s}^{-1}$ and again take the same values of G , ρ and D_p . We then find $r_{\text{ice}} > 3-25 \text{ m}$ corresponding to the fractional area of (sub)surface ice $\sim 0.001-0.05 \%$. This value is 10 times smaller than, or comparable with those of Vesta ($\gtrsim 0.01\%$, Palmer et al. 2017) and S-type Oort Cloud object (0.04 to 0.1%, Meech et al. 2016). These give a crude but useful estimation, by showing that even a tiny (sub)surface ice coverage can release the meteoroid-sized particles. Yet note that no exposed water ice is observed on 2003 YT₁. Note also that it is difficult to detect subsurface ice by observations. Laboratory data find that even a few mm thickness crust (organic mantle) perfectly attenuates the near-infrared absorption band depths of the subsurface water ice (Poch et al. 2016). Spacecraft missions for excavations alike NASA's Deep Impact (A'Hearn et al. 2005; Kasuga et al. 2006, 2007) and JAXA's Hayabusa2 (Watanabe et al. 2017) would be advantageous for the detection in the km-scale NEAs. Until then sublimation of water ice is, at least, remained as a potential dust production mechanism for 2003 YT₁.

Briefly we have examined a variety of process capable of launching dust particles from 2003 YT₁. Rotational instability, impacts and radiation pressure can produce mm to cm-scale dust particles. By contrast, resurfacing and photoionization are implausible. Insufficient evidence exists in thermal fracture and sublimation of ice, going to future work.

5. SUMMARY

We present SonotaCo meteor survey of a fireball taken in Japan on UT 2017 April 28 at 15^h 58^m 19^s. The data is measured for orbit and physical properties. Specific detections give the following results.

1. Radiant point, geocentric velocity and orbital elements of fireball are determined. The similarity to asteroid 2003 YT₁ with D-criterions (cf. $D_{\text{SH}} = 0.0079$) gives an order of smaller values than the significant threshold, indicating a parental association.
2. Absolute visual magnitude is $M_v = -4.10 \pm 0.42$ mag. Light curves give the meteoroid mass $m = 29 \pm 1$ g which corresponds to the size $a_s = 2.7 \pm 0.1$ cm with the density 2700 kg m^{-3} .
3. Meteor luminous model comprising time derivative of momentum in drag equation is suggested to employ a velocity-dependent ablation coefficient, as determined by $\sigma v^2 < 1$.
4. The 2003 YT₁ binary could be rotationally disrupted asteroids with mass shedding, consistent with [Pravec & Harris \(2007\)](#). The YORP spin-up timescale is $\tau_Y \sim 2$ Myr, shortly induces rotational instability. The resulting end-state is a breakup/fission if it is the rubble-piled body held by weak cohesive strength $S_c \sim 240 \text{ N m}^{-2}$.
5. Micrometeorite impactors with $\simeq 1$ mm in size sufficiently produce the cm-sized dust particles, given populated near the 2003 YT₁ orbit.
6. Radiation pressure may sweep out the mm-sized particles from 2003 YT₁, could be source of faint meteors with apparent magnitude of $\sim +5$ mag. The cm-sized particles are too large to be removed.
7. The other dust production mechanisms are unprovable or pending.

We are grateful to SonotaCo for support. We appreciate Hideaki Muroishi, Hiroshi Yamakawa, Kazuhiko Yoneguchi, Naoya Saito, Hiroyuki Inoue, Chikara Shimoda, Toshio Kamimura and Koji Okano for data contributions. We acknowledge Masahisa Yanagisawa, David Čapek, Takaya Okamoto and David Jewitt for discussion, and David Asher for review. TK gives special thanks to Petr Pravec for presentation source and to Daniel J. Scheeres for scientific editor. Finally, we express a deep gratitude to Juraj Tóth and his LOC members of Meteoroids 2019 held in Bratislava, Slovakia for providing opportunity to enhance this study.

Facilities: SonotaCo Network, EDMOND

Software: UFOCaptureHD2, UFOOrbitV2, UFOAnalyzerV2 ([SonotaCo 2009](#); [SonotaCo et al. 2014](#); [SonotaCo 2016, 2017](#))

APPENDIX

REFERENCES

- | | |
|---|--|
| Abell, P. A., Gaffey, M. J., & Hardersen, P. S.
2004, in Bulletin of the American Astronomical Society, Vol. 36, AAS/Division for Planetary Sciences Meeting Abstracts #36, 1132 | Abell, P. A., Gaffey, M. J., Hardersen, P. S., et al.
2005, in Bulletin of the American Astronomical Society, Vol. 37, AAS/Division for Planetary Sciences Meeting Abstracts #37, 627 |
|---|--|

- Agarwal, J., Jewitt, D., & Weaver, H. 2013, *ApJ*, 769, 46
- Agarwal, J., A'Hearn, M. F., Vincent, J. B., et al. 2016, *MNRAS*, 462, S78
- Agarwal, J., Della Corte, V., Feldman, P. D., et al. 2017, *MNRAS*, 469, s606
- A'Hearn, M. F., Belton, M. J. S., Delamere, W. A., et al. 2005, *Science*, 310, 258
- Asher, D. J., Clube, S. V. M., & Steel, D. I. 1993, *MNRAS*, 264, 93
- Binzel, R. P., Morbidelli, A., Merouane, S., et al. 2010, *Nature*, 463, 331
- Bottke, W. F., Nolan, M. C., Greenberg, R., & Kolvoord, R. A. 1994, in *Hazards Due to Comets and Asteroids*, ed. T. Gehrels, M. S. Matthews, & A. M. Schumann (University of Arizona Press, Tucson), 337–357
- Bottke, W. F., Morbidelli, A., Jedicke, R., et al. 2002, *Icarus*, 156, 399
- Bronshten, V. A. 1983, Physics of meteoric phenomena from the Russian
- Brooks, H. E. 2006, in *Bulletin of the American Astronomical Society*, Vol. 38, American Astronomical Society Meeting Abstracts, 934
- Brown, P., Marchenko, V., Moser, D. E., Weryk, R., & Cooke, W. 2013, *Meteoritics and Planetary Science*, 48, 270
- Burbine, T. H., Buchanan, P. C., Dolkar, T., & Binzel, R. P. 2009, *Meteoritics and Planetary Science*, 44, 1331
- Carrillo-Sánchez, J. D., Plane, J. M. C., Feng, W., Nesvorný, D., & Janches, D. 2015, *Geophys. Res. Lett.*, 42, 6518
- Ceplecha, Z., Borovička, J., Elford, W. G., et al. 1998, *SSRv*, 84, 327
- Ceplecha, Z., & McCrosky, R. E. 1976, *J. Geophys. Res.*, 81, 6257
- Ceplecha, Z., & Revelle, D. O. 2005, *Meteoritics and Planetary Science*, 40, 35
- Ceplecha, Z., Spurný, P., Borovicka, J., & Keclíkova, J. 1993, *A&A*, 279, 615
- Chandler, C. O., Kueny, J., Gustafsson, A., et al. 2019, *ApJL*, 877, L12
- Chang, C.-K., Ip, W.-H., Lin, H.-W., et al. 2015, *ApJS*, 219, 27
- Clark, D. L., Wiegert, P., & Brown, P. G. 2019, *MNRAS*, 487, L35
- Cochran, A. L., Vilas, F., Jarvis, K. S., & Kelley, M. S. 2004, *Icarus*, 167, 360
- Cruikshank, D. P., Tholen, D. J., Hartmann, W. K., Bell, J. F., & Brown, R. H. 1991, *Icarus*, 89, 1
- Davis, D. R., Durda, D. D., Marzari, F., Campo Bagatin, A., & Gil-Hutton, R. 2002, in *Asteroids III*, W. F. Bottke Jr., A. Cellino, P. Paolicchi, and R. P. Binzel (eds), University of Arizona Press, Tucson, p.545-558, 545–558
- De Sanctis, M. C., Combe, J. P., Ammannito, E., et al. 2012, *ApJ*, 758, L36
- Delbo, M., Walsh, K., Mueller, M., Harris, A. W., & Howell, E. S. 2011, *Icarus*, 212, 138
- Denevi, B. W., Coman, E. I., Blewett, D. T., et al. 2012, in *Lunar and Planetary Science Conference*, 1943
- Drummond, J. D. 1981, *Icarus*, 45, 545
- Dumitru, B. A., Birlan, M., Popescu, M., & Nedelcu, D. A. 2017, *A&A*, 607, A5
- Fang, J., & Margot, J.-L. 2012, *AJ*, 143, 24
- Flynn, G. J., Consolmagno, G. J., Brown, P., & Macke, R. J. 2018, *Chemie der Erde / Geochemistry*, 78, 269
- Flynn, G. J., & Durda, D. D. 2004, *Planet. Space Sci.*, 52, 1129
- Fu, R. R., Hager, B. H., Ermakov, A. I., & Zuber, M. T. 2014, *Icarus*, 240, 133
- Fulle, M., Ivanovski, S. L., Bertini, I., et al. 2015, *A&A*, 583, A14
- Fulvio, D., Perna, D., Ieva, S., et al. 2016, *MNRAS*, 455, 584
- Galád, A., Gajdoš, S., Kornoš, L., Vilagi, J., & Pravec, P. 2004, *International Astronomical Union Circular*, 8336, 4
- Gliazzo, M. A., Silber, E. A., & Bancelin, D. 2017, *Astronomische Nachrichten*, 338, 375
- Goldreich, P., & Sari, R. 2009, *ApJ*, 691, 54
- Graves, K. J., Minton, D. A., Hirabayashi, M., DeMeo, F. E., & Carry, B. 2018, *Icarus*, 304, 162
- Graves, K. J., Minton, D. A., Molnar, J. L., & Hirabayashi, M. 2019, *Icarus*, 322, 1
- Graykowski, A., & Jewitt, D. 2019, *AJ*, 158, 112
- Haack, H., Rasmussen, K. L., & Warren, P. H. 1990, *J. Geophys. Res.*, 95, 5111
- Hasegawa, S., Murakawa, K., Ishiguro, M., et al. 2003, *Geophys. Res. Lett.*, 30, 2123
- Hicks, M., Somers, J., Barajas, T., et al. 2009, *The Astronomer's Telegram*, 2289
- Hirabayashi, M., Scheeres, D. J., Sánchez, D. P., & Gabriel, T. 2014, *ApJL*, 789, L12

- Hoffmann, M., Nathues, A., Vincent, J. B., & Sierks, H. 2012, in EGU General Assembly Conference Abstracts, Vol. 14, 5530
- Housen, K. R., & Holsapple, K. A. 2011, Icarus, 211, 856
- Hu, X., Shi, X., Sierks, H., et al. 2017, MNRAS, 469, S295
- Hui, M.-T., Kim, Y., & Gao, X. 2019, MNRAS, 488, L143
- Hui, M.-T., & Li, J. 2017, AJ, 153, 23
- Ieva, S., Dotto, E., Lazzaro, D., et al. 2016, MNRAS, 455, 2871
- Jacobson, S. A., & Scheeres, D. J. 2011, ApJ, 736, L19
- Janches, D., Plane, J. M. C., Nesvorný, D., et al. 2014, ApJ, 796, 41
- Jeffers, S. V., Manley, S. P., Bailey, M. E., & Asher, D. J. 2001, MNRAS, 327, 126
- Jenniskens, P. 2017, Planet. Space Sci., 143, 116
- Jenniskens, P., & Lyytinen, E. 2005, AJ, 130, 1286
- Jewitt, D. 2012, AJ, 143, 66
- . 2013, AJ, 145, 133
- Jewitt, D., Agarwal, J., Li, J., et al. 2014a, ApJL, 784, L8
- . 2017, AJ, 153, 223
- Jewitt, D., Asmus, D., Yang, B., & Li, J. 2019a, AJ, 157, 193
- Jewitt, D., Hsieh, H., & Agarwal, J. 2015, in Asteroids IV, ed. P. Michel, F. E. DeMeo, & W. F. Bottke (University of Arizona Press), 221–241
- Jewitt, D., Ishiguro, M., & Agarwal, J. 2013, ApJL, 764, L5
- Jewitt, D., Ishiguro, M., Weaver, H., et al. 2014b, AJ, 147, 117
- Jewitt, D., Kim, Y., Luu, J., et al. 2019b, ApJL, 876, L19
- Jewitt, D., & Li, J. 2010, AJ, 140, 1519
- Jewitt, D., Mutchler, M., Agarwal, J., & Li, J. 2018, AJ, 156, 238
- Jewitt, D., Weaver, H., Agarwal, J., Mutchler, M., & Drahus, M. 2010, Nature, 467, 817
- Jin, Z., & Bose, M. 2019, Science Advances, 5, doi:10.1126/sciadv.aav8106
- Jutzi, M., Michel, P., Benz, W., & Richardson, D. C. 2010, Icarus, 207, 54
- Kasuga, T., & Jewitt, D. 2019, in Meteoroids: Sources of Meteors on Earth and Beyond, Ryabova G. O., Asher D. J., and Campbell-Brown M. D. (eds.), Cambridge, UK: Cambridge University Press, 336 pp., ISBN 9781108426718, 2019, p. 187–209, 187
- Kasuga, T., Sato, M., & Watanabe, J. 2007, Advances in Space Research, 40, 215
- Kasuga, T., Watanabe, J.-I., & Sato, M. 2006, MNRAS, 373, 1107
- Kleyna, J. T., Hainaut, O. R., Meech, K. J., et al. 2019, ApJL, 874, L20
- Kornoš, L., Koukal, J., Piffl, R., & Tóth, J. 2014a, in Proceedings of the International Meteor Conference, Poznan, Poland, 22–25 August 2013, ed. M. Gyssens, P. Roggemans, & P. Zoladek, 23–25
- Kornoš, L., Matlovič, P., Rudawska, R., et al. 2014b, in Meteoroids 2013, ed. T. J. Jopek, F. J. M. Rietmeijer, J. Watanabe, & I. P. Williams, 225–233
- Küppers, M. 2019, Journal of Geophysical Research (Planets), 124, 205
- Larson, S. M., Grauer, A. D., Beshore, E., et al. 2004, in Bulletin of the American Astronomical Society, Vol. 36, AAS/Division for Planetary Sciences Meeting Abstracts #36, 1139
- Lauriello, P. 1974, International Journal of Rock Mechanics and Mining Sciences & Geomechanics Abstracts, 11, 75
- Lindblad, B. A. 1987, in The Evolution of the Small Bodies of the Solar System, ed. M. Fulchignoni & L. Kresak, 229
- Madiedo, J. M., Trigo-Rodríguez, J. M., Ortiz, J. L., Castro-Tirado, A. J., & Cabrera-Caño, J. 2014, MNRAS, 443, 1643
- Madiedo, J. M., Trigo-Rodríguez, J. M., Williams, I. P., Ortiz, J. L., & Cabrera, J. 2013, MNRAS, 431, 2464
- Mainzer, A., Grav, T., Bauer, J., et al. 2011, ApJ, 743, 156
- Mainzer, A., Grav, T., Masiero, J., et al. 2012, ApJ, 760, L12
- Margot, J. L., Pravec, P., Taylor, P., Carry, B., & Jacobson, S. 2015, in Asteroids IV, Patrick Michel, Francesca E. DeMeo, and William F. Bottke (eds.), University of Arizona Press, Tucson, 895 pp. ISBN: 978-0-816-53213-1, 2015., p.355-374, 355–374

- Marsset, M., DeMeo, F., Sonka, A., et al. 2019, *ApJL*, 882, L2
- Meech, K. J., Yang, B., Kleyna, J., et al. 2016, *Science Advances*, 2, e1600038
- Molaro, J. L., Byrne, S., & Langer, S. A. 2015, *Journal of Geophysical Research (Planets)*, 120, 255
- Morbidelli, A., Bottke, W. F., Jr., Froeschlé, C., & Michel, P. 2002, in *Asteroids III*, W. F. Bottke Jr., A. Cellino, P. Paolicchi, and R. P. Binzel (eds.), University of Arizona Press, Tucson, p.409-422, 409–422
- Moreno, F., Jehin, E., Licandro, J., et al. 2019, *A&A*, 624, L14
- Moskovitz, N. A., Fatka, P., Farnocchia, D., et al. 2019, *Icarus*, 333, 165
- Myers, J. R., Sande, C. B., Miller, A. C., Warren, W. H., Jr., & Tracewell, D. A. 2001, *VizieR Online Data Catalog*, V/109
- Nagasawa, K. 1981, *The Earth Monthly*, 3, 588
- Neslusan, L., Svoren, J., & Porubcan, V. 1998, *A&A*, 331, 411
- Nesvorný, D., Jenniskens, P., Levison, H. F., et al. 2010, *ApJ*, 713, 816
- Nolan, M. C., Howell, E. S., & Hine, A. A. 2004a, *IAUC*, 8336
- Nolan, M. C., Howell, E. S., & Miranda, G. 2004b, in *Bulletin of the American Astronomical Society*, Vol. 36, AAS/Division for Planetary Sciences Meeting Abstracts #36, 1132
- Olech, A., Źoładek, P., Wiśniewski, M., et al. 2017, *MNRAS*, 469, 2077
- Palmer, E. M., Heggy, E., & Kofman, W. 2017, *Nature Communications*, 8, 409
- Pariseau, G. W. 2006, *Design Analysis in Rock Mechanics* (London: Taylor and Francis), 576
- Pieters, C. M., Ammannito, E., Blewett, D. T., et al. 2012, *Nature*, 491, 79
- Poch, O., Pommerol, A., Jost, B., et al. 2016, *Icarus*, 267, 154
- Popova, O., Borovička, J., & Campbell-Brown, M. D. 2019, in *Meteoroids: Sources of Meteors on Earth and Beyond*, Ryabova G. O., Asher D. J., and Campbell-Brown M. D. (eds.), Cambridge, UK: Cambridge University Press, 336 pp., ISBN 9781108426718, 2019, p. 9-36, 9
- Pravec, P. 2005, *Society for Astronomical Sciences Annual Symposium*, 24, 61
- Pravec, P., & Harris, A. W. 2007, *Icarus*, 190, 250
- Pravec, P., Harris, A. W., Vokrouhlický, D., et al. 2008, *Icarus*, 197, 497
- Pravec, P., Scheirich, P., Kušnírák, P., et al. 2016, *Icarus*, 267, 267
- Richter, D., & Simmons, G. 1974, *International Journal of Rock Mechanics and Mining Sciences & Geomechanics Abstracts*, 11, 403
- Rivkin, A. S., Campins, H., Emery, J. P., et al. 2015, in *Asteroids IV*, Patrick Michel, Francesca E. DeMeo, and William F. Bottke (eds.), University of Arizona Press, Tucson, 895 pp. ISBN: 978-0-816-53213-1, 2015., p.65-87, 65–87
- Rivkin, A. S., Howell, E. S., Emery, J. P., & Sunshine, J. 2018, *Icarus*, 304, 74
- Rozitis, B., & Green, S. F. 2013, *MNRAS*, 430, 1376
- Rudawska, R., & Jenniskens, P. 2014, in *Meteoroids 2013*, ed. T. J. Jopek, F. J. M. Rietmeijer, J. Watanabe, & I. P. Williams, 217–224
- Russell, C. T., McSween, H. Y., Jaumann, R., & Raymond, C. A. 2015, in *Asteroids IV*, Patrick Michel, Francesca E. DeMeo, and William F. Bottke (eds.), University of Arizona Press, Tucson, 895 pp. ISBN: 978-0-816-53213-1, 2015., p.419-432, 419–432
- Russell, C. T., Raymond, C. A., Jaumann, R., et al. 2013, *Meteoritics and Planetary Science*, 48, 2076
- Sanchez, J. A., Michelsen, R., Reddy, V., & Nathues, A. 2013, *Icarus*, 225, 131
- Sato, M., & Watanabe, J. 2014, *Meteoroids 2013*, 329
- Scheeres, D. J., Hartzell, C. M., Sánchez, P., & Swift, M. 2010, *Icarus*, 210, 968
- Scheeres, D. J., & Sánchez, P. 2018, *Progress in Earth and Planetary Science*, 5, 25
- SonotaCo. 2009, *WGN, Journal of the International Meteor Organization*, 37, 55
- . 2016, *WGN, Journal of the International Meteor Organization*, 44, 42
- . 2017, *WGN, Journal of the International Meteor Organization*, 45, 95
- SonotaCo, Shimoda, C., Inoue, H., Masuzawa, T., & Sato, M. 2014, *WGN, Journal of the International Meteor Organization*, 42, 222
- Southworth, R. B., & Hawkins, G. S. 1963, *Smithsonian Contributions to Astrophysics*, 7, 261

- Spurný, P., Borovička, J., Mucke, H., & Svoreň, J. 2017, *A&A*, 605, A68
- Subasinghe, D., & Campbell-Brown, M. 2018, *AJ*, 155, 88
- Svetsov, V., Shuvalov, V., Collins, G., & Popova, O. 2019, in Meteoroids: Sources of Meteors on Earth and Beyond, Ryabova G. O., Asher D. J., and Campbell-Brown M. D. (eds.), Cambridge, UK: Cambridge University Press, 336 pp., ISBN 9781108426718, 2019, p. 275-298, 275
- Tancredi, G., Fernández, J. A., Rickman, H., & Licandro, J. 2006, *Icarus*, 182, 527
- Tichy, M., Kocer, M., Yeung, W. K. Y., et al. 2003, Minor Planet Electronic Circulars, 2003-Y30
- Tsuchiya, C., Sato, M., Watanabe, J.-i., et al. 2017, *Planet. Space Sci.*, 143, 142
- Vaubaillon, J., Neslušan, L., Sekhar, A., Rudawska, R., & Ryabova, G. O. 2019, From Parent Body to Meteor Shower: The Dynamics of Meteoroid Streams, 161
- Vokrouhlický, D., Bottke, W. F., Chesley, S. R., Scheeres, D. J., & Statler, T. S. 2015, in Asteroids IV, ed. F. E. D. Patrick Michel & W. F. Bottke (University of Arizona Press, Tucson), 509–531
- Walsh, K. J., & Jacobson, S. A. 2015, in Asteroids IV, Patrick Michel, Francesca E. DeMeo, and William F. Bottke (eds.), University of Arizona Press, Tucson, 895 pp. ISBN: 978-0-816-53213-1, 2015., p.375-393, 375–393
- Walsh, K. J., Richardson, D. C., & Michel, P. 2008, *Nature*, 454, 188
- Warner, B., Pravec, P., & Harris, A. P. 2018, NASA Planetary Data System
- Warner, B. D., Harris, A. W., & Pravec, P. 2009, *Icarus*, 202, 134
- Watanabe, S.-i., Tsuda, Y., Yoshikawa, M., et al. 2017, *SSRv*, 208, 3
- Weryk, R. J., & Brown, P. G. 2013, *Planet. Space Sci.*, 81, 32
- Williams, I. P., Jopek, T. J., Rudawska, R., Tóth, J., & Kornoš, L. 2019, in Meteoroids: Sources of Meteors on Earth and Beyond, Ryabova G. O., Asher D. J., and Campbell-Brown M. D. (eds.), Cambridge, UK: Cambridge University Press, 336 pp., ISBN 9781108426718, 2019, p. 210-234, 210
- Yamamoto, T. 1985, *A&A*, 142, 31
- Ye, Q., Kelley, M. S. P., Bodewits, D., et al. 2019, *ApJL*, 874, L16
- Ye, Q.-Z., Brown, P. G., & Pokorný, P. 2016, *MNRAS*, 462, 3511

APPENDIX

A. METEOR SEARCH IN SONOTACO AND EDMOND DATABASES

We used the SonotaCo and EDMOND databases to find other probable meteors which could be orbitally associated with asteroid 2003 YT₁ and the Kyoto fireball. Note that slow-speed meteors infer large uncertainties in the radiant points (Sato & Watanabe 2014; Tsuchiya et al. 2017), while the databases include little or nothing about estimations for errors on orbital information. Hence based on the asteroidal solar longitudes and radiant points in Table 2, we set the wide search ranges $\lambda_s - 30^\circ \leq \lambda'_s \leq \lambda_s + 30^\circ$, $\alpha - 30^\circ \leq \alpha' \leq \alpha + 30^\circ$, $\delta - 20^\circ \leq \delta' \leq \delta + 20^\circ$ and $v_g < 35 \text{ km s}^{-1}$ at descending or ascending node respectively. In which λ'_s , α' and δ' are those of meteors in the databases. Among them we take any of D-criterion for either the asteroid or the fireball presents the value of < 0.2 . Selected meteors are shown in Tables 8 and 9. The scattered results may not be sufficient to be part of the association.

B. METEOR LUMINOUS MODEL

We present a procedure to develop a new meteor luminous model based on the classical model (Bronshten 1983; Ceplecha et al. 1998) (Reviewed in Popova et al. 2019). The meteoroid kinetic energy is transformed into radiation during the meteor flight. The classical luminous model equating mass loss (ablation), luminosity and deceleration is given by (Chapter 3.4 in Ceplecha et al. 1998),

$$\begin{aligned} I &= -\tau \frac{d}{dt} \left(\frac{mv^2}{2} \right) \\ &= -\tau \left(\frac{v^2}{2} \frac{dm}{dt} + mv \frac{dv}{dt} \right) \end{aligned} \quad (\text{B1})$$

$$= -\tau \left(1 + \frac{2}{\sigma v^2} \right) \frac{v^2}{2} \frac{dm}{dt}, \quad (\text{B2})$$

where I is the meteor luminosity, τ is the luminous efficiency, m is the meteoroid mass (g), σ is the ablation coefficient ($\text{s}^2 \text{ km}^{-2}$) ($= \text{kg MJ}^{-1}$), v is the meteor velocity (cm s^{-1}) and t (s) is time. The meteor luminosity is defined as $I = 10^{-0.4M_v}$ in magnitude-based units in the visual region, where M_v is the absolute magnitude in 100 km distance. The ablation coefficient is generally defined as $\sigma = \Lambda/2Q\Gamma$, where Λ is the heat transfer coefficient, Q is the energy necessary to ablate an unit mass of meteoroid (MJ kg^{-1}) and Γ is the drag coefficient. The motion and ablation of single non-fragmenting body through the atmosphere has been traditionally represented by the drag and mass-loss equations as (Chapter 3.2 in Ceplecha et al. 1998),

$$m \frac{dv}{dt} = -\Gamma S \rho_a v^2, \quad (\text{B3})$$

$$\frac{dm}{dt} = -\frac{\Lambda S}{2Q} \rho_a v^3, \quad (\text{B4})$$

respectively. Here S is the cross-section of meteoroid and ρ_a is the atmospheric density. The Equations (B3) and (B4) are related as

$$\frac{dv}{dt} = \frac{1}{\sigma m v} \frac{dm}{dt}. \quad (\text{B5})$$

Substitution Equation (B5) into (B1), we obtain the classical luminous model in Equation (B2).

A new luminous model is developed by refining the drag equation (B3). Since the ablation process can lose the mass of meteoroid itself, the drag force should be expressed in differential form of the momentum ([Nagasawa 1981](#), in Japanese). The drag equation (B3) thus can be rewritten as

$$\frac{d}{dt}(mv) = m\frac{dv}{dt} + \frac{dm}{dt}v = -\Gamma S \rho_a v^2. \quad (\text{B6})$$

Substitution Equation (B4) into (B6), the refined drag equation is obtained as

$$m\frac{dv}{dt} = -\Gamma S \rho_a v^2(1 - \sigma v^2), \quad (\text{B7})$$

where $\sigma v^2 < 1$ is required. The new relation between dv/dt and dm/dt using Equations (B4) and (B7) finds

$$\frac{dv}{dt} = \frac{1 - \sigma v^2}{\sigma mv} \frac{dm}{dt}. \quad (\text{B8})$$

By substituting Equation (B8) into (B1), we obtain the new luminous model

$$I = -\tau \left(\frac{2}{\sigma v^2} - 1 \right) \frac{v^2}{2} \frac{dm}{dt}. \quad (\text{B9})$$

The ablation coefficient, σ , characterizes the ability of meteoroid to ablate. A larger value produces higher mass-loss, resulting in brighter luminosity. The estimated values in the published literature are, however, highly scattered and inconclusive. The distribution of coefficient (single-body theory) showing $0.01 < \sigma < 0.6 \text{ s}^2 \text{ km}^{-2}$ is used to classify the meteoroid type, such as ordinary ($0.014 \text{ s}^2 \text{ km}^{-2}$), carbonaceous chondrites ($0.042 \text{ s}^2 \text{ km}^{-2}$) or soft cometary materials ($0.21 \text{ s}^2 \text{ km}^{-2}$) and so on ([Ceplecha et al. 1993](#)). Later, on the contrary, fragmentation process is suggested to be dominant for mass loss, finding the low $\sigma = 0.004$ to $0.008 \text{ s}^2 \text{ km}^{-2}$ in any type of meteorite ([Ceplecha & Revelle 2005](#)). But the process also depends on the assumed models. The works are reviewed in more detail by [Popova et al. \(2019\)](#).

Here, we propose an appropriate ablation coefficient for the new luminous model therein. It concisely depends on meteor velocity, as determined by $\sigma v^2 < 1$ (see Equation (B7)). Setting $v=23.7 \text{ km s}^{-1}$ (fireball) finds $\sigma < 0.00178 \text{ s}^2 \text{ km}^{-2}$. We thus use $\sigma = 0.0017 \text{ s}^2 \text{ km}^{-2}$ for this study.

Table 1. The Kyoto Fireball Trajectory

	Longitude (deg E)	Latitude (deg N)	Height (km)
Beginning	136.0156 ± 0.0004	35.4275 ± 0.0005	88.80 ± 0.07
End	135.4746 ± 0.0002	34.9859 ± 0.0003	47.80 ± 0.04

NOTE—The atmospheric trajectory for the fireball (UT 2017 April 28) are determined by five camera measurements. The observing IDs are TK8_S7, Osaka03_3N, Osaka03_06^a, IS2_S and IS5_SW (see Figure 1). The orbital properties (e.g the elements), speed and positioning accuracy (cf. section 2) give the estimation of uncertainties.

^aThe location: Osaka03 obtained the fireball data with two cameras which are expressed as Osaka03_3N and Osaka03_06 respectively.

Table 2. Radiant Point and Geocentric Velocity

Object	α^a (deg)	δ^b (deg)	v_g^c (km s ⁻¹)	Δr^d (AU)	λ_s^e (deg)	UT Date
Fireball	321.2 ± 0.5	$+51.2 \pm 0.3$	23.7 ± 0.5	-	38.3150	Apr 28.7, 2017
2003 YT ₁	320.54	+50.97	23.7	0.0026	38.3333	Apr 28.7, 2017
	87.30	-36.10	23.7	0.0279	218.3331	Oct 31.8, 2017

NOTE— Radiant point and geocentric velocity of 2003 YT₁ are calculated by the parallel shift of moving vector at each orbital node (method (*P*) in Neslusan et al. 1998). The descending node is at $\lambda_s=38.3333^\circ$ (Apr 28.7, 2017) and the ascending node is at $\lambda_s=218.3331^\circ$ (Oct 31.8, 2017).

^aRight ascension (J2000.0).

^bDeclination (J2000.0).

^cGeocentric velocity.

^dDistance from descending/ascending node to the Earth's orbit.

^eSolar longitude (J2000.0).

Table 3. Orbital Elements and Period

Object	a^a (AU)	e^b	i^c (deg)	q^d (AU)	ω^e (deg)	Ω^f (deg)	P_{orb}^g (yr)
Fireball	1.111 ± 0.016	0.297 ± 0.004	43.9 ± 0.9	0.781 ± 0.007	91.2 ± 2.7	38.315 ± 0.001	1.17
2003 YT ₁	1.110	0.292	44.1	0.786	91.0	38.335	1.17

NOTE—The uncertainties are propagated from those of radiant point and geocentric velocity (Table 2) through the Monte-Carlo technique. Orbital data of 2003 YT₁ are obtained from NASA JPL Small-Body Database Brower (2018).

*a*Semimajor axis.

*b*Eccentricity.

*c*Inclination.

*d*Perihelion distance.

*e*Argument of perihelion.

*f*Longitude of ascending node.

*g*Orbital period.

Table 4. Tokyo Data (ID: TK8_S7)

N	H^a	L_D^b	$m(\text{obs})^c$	M_v^d	I^e	m_N^f
1	82.46 ± 0.12	351.1	2.33 ± 0.50	-0.40 ± 0.50	1.45 ± 0.67	0.016 ± 0.007
2	81.95 ± 0.12	351.6	1.96 ± 0.50	-0.77 ± 0.50	2.03 ± 0.94	0.023 ± 0.011
3	81.72 ± 0.12	351.8	2.16 ± 0.50	-0.57 ± 0.50	1.69 ± 0.78	0.018 ± 0.008
4	81.25 ± 0.12	352.3	1.52 ± 0.50	-1.21 ± 0.50	3.05 ± 1.40	0.034 ± 0.016
5	80.82 ± 0.12	352.8	1.58 ± 0.50	-1.16 ± 0.50	2.91 ± 1.34	0.032 ± 0.015
6	80.63 ± 0.12	353.0	1.24 ± 0.50	-1.50 ± 0.50	3.98 ± 1.83	0.044 ± 0.020
7	80.37 ± 0.12	353.2	0.60 ± 0.50	-2.14 ± 0.50	7.18 ± 3.31	0.079 ± 0.036
8	80.20 ± 0.12	353.4	0.69 ± 0.50	-2.05 ± 0.50	6.61 ± 3.04	0.073 ± 0.034
9	79.95 ± 0.12	353.7	0.61 ± 0.50	-2.13 ± 0.50	7.11 ± 3.28	0.079 ± 0.037
10	79.68 ± 0.12	353.9	0.77 ± 0.50	-1.97 ± 0.50	6.14 ± 2.83	0.068 ± 0.031
11	79.51 ± 0.12	354.1	0.82 ± 0.50	-1.93 ± 0.50	5.92 ± 2.72	0.066 ± 0.030
12	79.23 ± 0.12	354.4	0.58 ± 0.50	-2.17 ± 0.50	7.38 ± 3.40	0.081 ± 0.037
13	79.07 ± 0.12	354.6	0.66 ± 0.50	-2.09 ± 0.50	6.85 ± 3.16	0.076 ± 0.035
14	78.84 ± 0.12	354.8	0.34 ± 0.50	-2.41 ± 0.50	9.20 ± 4.24	0.101 ± 0.047
15	78.60 ± 0.12	355.1	0.35 ± 0.50	-2.40 ± 0.50	9.12 ± 4.20	0.100 ± 0.047
16	78.37 ± 0.12	355.3	-0.07 ± 0.50	-2.82 ± 0.50	13.43 ± 6.18	0.149 ± 0.069
17	78.15 ± 0.12	355.6	0.15 ± 0.50	-2.60 ± 0.50	10.96 ± 5.05	0.121 ± 0.057
18	77.93 ± 0.12	355.8	0.03 ± 0.50	-2.73 ± 0.50	12.36 ± 5.69	0.137 ± 0.063
19	77.70 ± 0.12	356.0	-0.19 ± 0.50	-2.95 ± 0.50	15.14 ± 6.97	0.167 ± 0.078
20	77.49 ± 0.12	356.3	-0.18 ± 0.50	-2.94 ± 0.50	15.00 ± 6.91	0.166 ± 0.077
21	77.28 ± 0.12	356.5	-0.10 ± 0.50	-2.86 ± 0.50	13.93 ± 6.42	0.154 ± 0.071
22	77.02 ± 0.12	356.7	-0.33 ± 0.50	-3.09 ± 0.50	17.22 ± 7.93	0.190 ± 0.088
23	76.83 ± 0.12	357.0	-0.16 ± 0.50	-2.92 ± 0.50	14.72 ± 6.78	0.163 ± 0.075
24	76.59 ± 0.12	357.2	-0.07 ± 0.50	-2.83 ± 0.50	13.55 ± 6.24	0.150 ± 0.070
25	76.41 ± 0.12	357.4	-0.09 ± 0.50	-2.86 ± 0.50	13.93 ± 6.42	0.154 ± 0.071
26	76.15 ± 0.12	357.7	-0.20 ± 0.50	-2.97 ± 0.50	15.42 ± 7.10	0.171 ± 0.079
27	75.89 ± 0.12	358.0	-0.10 ± 0.50	-2.87 ± 0.50	14.06 ± 6.48	0.155 ± 0.072
28	75.74 ± 0.13	358.1	-0.39 ± 0.50	-3.16 ± 0.50	18.37 ± 8.46	0.203 ± 0.095
29	75.50 ± 0.13	358.4	-0.57 ± 0.50	-3.34 ± 0.50	21.68 ± 9.98	0.239 ± 0.111
30	75.27 ± 0.13	358.6	-0.45 ± 0.50	-3.22 ± 0.50	19.41 ± 8.94	0.215 ± 0.100
31	75.02 ± 0.13	358.9	-0.43 ± 0.50	-3.20 ± 0.50	19.05 ± 8.77	0.211 ± 0.098
32	74.82 ± 0.13	359.1	-0.22 ± 0.50	-3.00 ± 0.50	15.85 ± 7.30	0.175 ± 0.081
33	74.63 ± 0.13	359.3	-0.41 ± 0.50	-3.19 ± 0.50	18.88 ± 8.69	0.209 ± 0.097
34	74.41 ± 0.13	359.6	-0.45 ± 0.50	-3.23 ± 0.50	19.59 ± 9.02	0.216 ± 0.101
35	74.19 ± 0.13	359.8	-0.62 ± 0.50	-3.40 ± 0.50	22.91 ± 10.55	0.253 ± 0.117
36	73.97 ± 0.13	360.1	-0.53 ± 0.50	-3.31 ± 0.50	21.09 ± 9.71	0.233 ± 0.108
37	73.70 ± 0.13	360.3	-0.58 ± 0.50	-3.36 ± 0.50	22.08 ± 10.17	0.244 ± 0.113
38	73.49 ± 0.13	360.6	-0.71 ± 0.50	-3.50 ± 0.50	25.12 ± 11.57	0.278 ± 0.129
39	73.29 ± 0.13	360.8	-0.63 ± 0.50	-3.42 ± 0.50	23.33 ± 10.75	0.258 ± 0.119
40	73.10 ± 0.13	361.0	-0.71 ± 0.50	-3.50 ± 0.50	25.12 ± 11.57	0.278 ± 0.129

Table 4 continued on next page

Table 4 (*continued*)

N	H^a	L_D^b	$m(\text{obs})^c$	M_v^d	I^e	m_N^f
41	72.86 ± 0.13	361.3	-0.85 ± 0.50	-3.64 ± 0.50	28.58 ± 13.16	0.316 ± 0.147
42	72.65 ± 0.13	361.5	-0.77 ± 0.50	-3.56 ± 0.50	26.55 ± 12.22	0.293 ± 0.136
43	72.41 ± 0.13	361.8	-0.93 ± 0.50	-3.72 ± 0.50	30.76 ± 14.17	0.340 ± 0.158
44	72.24 ± 0.13	362.0	-1.04 ± 0.50	-3.83 ± 0.50	34.04 ± 15.68	0.376 ± 0.175
45	72.01 ± 0.13	362.2	-0.89 ± 0.50	-3.68 ± 0.50	29.65 ± 13.65	0.328 ± 0.152
46	71.82 ± 0.13	362.4	-0.94 ± 0.50	-3.74 ± 0.50	31.33 ± 14.43	0.346 ± 0.160
47	71.61 ± 0.13	362.7	-0.90 ± 0.50	-3.70 ± 0.50	30.20 ± 13.91	0.334 ± 0.155
48	71.39 ± 0.13	362.9	-0.96 ± 0.50	-3.76 ± 0.50	31.92 ± 14.70	0.353 ± 0.164
49	71.13 ± 0.13	363.2	-0.84 ± 0.50	-3.64 ± 0.50	28.58 ± 13.16	0.316 ± 0.147
50	70.96 ± 0.13	363.4	-0.73 ± 0.50	-3.53 ± 0.50	25.82 ± 11.89	0.286 ± 0.133
51	70.70 ± 0.13	363.7	-0.64 ± 0.50	-3.44 ± 0.50	23.77 ± 10.95	0.263 ± 0.122
52	70.49 ± 0.13	363.9	-0.78 ± 0.50	-3.58 ± 0.50	27.04 ± 12.45	0.299 ± 0.139
53	70.34 ± 0.13	364.1	-0.91 ± 0.50	-3.72 ± 0.50	30.76 ± 14.17	0.340 ± 0.158
54	70.11 ± 0.13	364.3	-0.77 ± 0.50	-3.58 ± 0.50	27.04 ± 12.45	0.299 ± 0.139
55	69.88 ± 0.13	364.6	-0.91 ± 0.50	-3.72 ± 0.50	30.76 ± 14.17	0.340 ± 0.158
56	69.65 ± 0.13	364.8	-0.72 ± 0.50	-3.53 ± 0.50	25.82 ± 11.89	0.286 ± 0.133
57	69.43 ± 0.13	365.1	-0.63 ± 0.50	-3.44 ± 0.50	23.77 ± 10.95	0.263 ± 0.122
58	69.18 ± 0.13	365.4	-0.72 ± 0.50	-3.53 ± 0.50	25.82 ± 11.89	0.286 ± 0.133
59	68.99 ± 0.13	365.6	-0.85 ± 0.50	-3.67 ± 0.50	29.38 ± 13.53	0.325 ± 0.151
60	68.66 ± 0.13	366.0	-0.71 ± 0.50	-3.53 ± 0.50	25.82 ± 11.89	0.286 ± 0.133
61	68.51 ± 0.13	366.1	-0.71 ± 0.50	-3.53 ± 0.50	25.82 ± 11.89	0.286 ± 0.133
62	68.28 ± 0.13	366.4	-0.74 ± 0.50	-3.56 ± 0.50	26.55 ± 12.22	0.293 ± 0.136
63	68.01 ± 0.13	366.7	-0.75 ± 0.50	-3.57 ± 0.50	26.79 ± 12.34	0.296 ± 0.138
64	67.83 ± 0.13	366.9	-0.53 ± 0.50	-3.35 ± 0.50	21.88 ± 10.08	0.242 ± 0.113
65	67.57 ± 0.13	367.2	-0.75 ± 0.50	-3.57 ± 0.50	26.79 ± 12.34	0.296 ± 0.138
66	67.34 ± 0.13	367.5	-0.80 ± 0.50	-3.63 ± 0.50	28.31 ± 13.04	0.313 ± 0.146
67	67.11 ± 0.13	367.7	-0.70 ± 0.50	-3.53 ± 0.50	25.82 ± 11.89	0.286 ± 0.133
68	66.93 ± 0.13	367.9	-0.62 ± 0.50	-3.45 ± 0.50	23.99 ± 11.05	0.265 ± 0.123
69	66.70 ± 0.13	368.2	-0.69 ± 0.50	-3.52 ± 0.50	25.59 ± 11.78	0.283 ± 0.131
70	66.48 ± 0.13	368.5	-0.80 ± 0.50	-3.63 ± 0.50	28.31 ± 13.04	0.313 ± 0.146
71	66.22 ± 0.13	368.8	-0.67 ± 0.50	-3.50 ± 0.50	25.12 ± 11.57	0.278 ± 0.129
72	66.04 ± 0.13	369.0	-1.05 ± 0.50	-3.89 ± 0.50	35.97 ± 16.57	0.397 ± 0.184
73	65.80 ± 0.13	369.2	-1.09 ± 0.50	-3.93 ± 0.50	37.33 ± 17.19	0.413 ± 0.192
74	65.60 ± 0.13	369.5	-1.09 ± 0.50	-3.93 ± 0.50	37.33 ± 17.19	0.413 ± 0.192
75	65.43 ± 0.13	369.7	-0.76 ± 0.50	-3.60 ± 0.50	27.54 ± 12.68	0.304 ± 0.141
76	65.21 ± 0.13	369.9	-0.80 ± 0.50	-3.64 ± 0.50	28.58 ± 13.16	0.316 ± 0.147
77	65.04 ± 0.13	370.1	-0.54 ± 0.50	-3.38 ± 0.50	22.49 ± 10.36	0.248 ± 0.115
78	64.83 ± 0.13	370.4	-0.48 ± 0.50	-3.32 ± 0.50	21.28 ± 9.80	0.236 ± 0.109
79	64.60 ± 0.13	370.6	-0.59 ± 0.50	-3.43 ± 0.50	23.55 ± 10.85	0.260 ± 0.121
80	64.44 ± 0.13	370.8	-0.80 ± 0.50	-3.65 ± 0.50	28.84 ± 13.28	0.319 ± 0.148
81	64.17 ± 0.13	371.1	-0.72 ± 0.50	-3.57 ± 0.50	26.79 ± 12.34	0.296 ± 0.138
82	63.85 ± 0.13	371.5	-0.69 ± 0.50	-3.54 ± 0.50	26.06 ± 12.00	0.288 ± 0.134
83	63.58 ± 0.13	371.8	-0.68 ± 0.50	-3.53 ± 0.50	25.82 ± 11.89	0.286 ± 0.133

Table 4 continued on next page

Table 4 (*continued*)

N	<i>H</i> ^a	<i>L</i> _D ^b	<i>m</i> (obs) ^c	<i>M</i> _v ^d	<i>I</i> ^e	<i>m</i> _N ^f
84	63.38 ± 0.13	372.1	-0.88 ± 0.50	-3.73 ± 0.50	31.05 ± 14.30	0.343 ± 0.159
85	63.17 ± 0.13	372.3	-0.71 ± 0.50	-3.56 ± 0.50	26.55 ± 12.22	0.293 ± 0.136
86	62.91 ± 0.13	372.6	-0.67 ± 0.50	-3.53 ± 0.50	25.82 ± 11.89	0.286 ± 0.133
87	62.75 ± 0.13	372.8	-0.65 ± 0.50	-3.51 ± 0.50	25.35 ± 11.67	0.280 ± 0.130
88	62.45 ± 0.13	373.2	-0.51 ± 0.50	-3.37 ± 0.50	22.28 ± 10.26	0.247 ± 0.115
89	62.28 ± 0.13	373.4	-0.69 ± 0.50	-3.55 ± 0.50	26.30 ± 12.11	0.290 ± 0.135
90	62.07 ± 0.13	373.6	-0.57 ± 0.50	-3.43 ± 0.50	23.55 ± 10.85	0.260 ± 0.121
91	61.81 ± 0.13	373.9	-0.64 ± 0.50	-3.50 ± 0.50	25.12 ± 11.57	0.278 ± 0.129
92	61.65 ± 0.13	374.1	-0.69 ± 0.50	-3.55 ± 0.50	26.30 ± 12.11	0.290 ± 0.135
93	61.38 ± 0.13	374.4	-0.39 ± 0.50	-3.26 ± 0.50	20.14 ± 9.27	0.223 ± 0.104
94	61.24 ± 0.13	374.6	-0.51 ± 0.50	-3.38 ± 0.50	22.49 ± 10.36	0.248 ± 0.115
95	60.99 ± 0.13	374.9	-0.48 ± 0.50	-3.35 ± 0.50	21.88 ± 10.08	0.242 ± 0.113
96	60.77 ± 0.13	375.2	-0.57 ± 0.50	-3.44 ± 0.50	23.77 ± 10.95	0.263 ± 0.122
97	60.54 ± 0.13	375.4	-0.71 ± 0.50	-3.58 ± 0.50	27.04 ± 12.45	0.299 ± 0.139
98	60.32 ± 0.13	375.7	-0.54 ± 0.50	-3.41 ± 0.50	23.12 ± 10.65	0.256 ± 0.119
99	60.14 ± 0.13	375.9	-0.36 ± 0.50	-3.24 ± 0.50	19.77 ± 9.10	0.218 ± 0.101
100	59.89 ± 0.13	376.2	-0.30 ± 0.50	-3.18 ± 0.50	18.71 ± 8.61	0.207 ± 0.096
101	59.75 ± 0.13	376.4	-0.59 ± 0.50	-3.47 ± 0.50	24.43 ± 11.25	0.270 ± 0.125
102	59.50 ± 0.13	376.7	-0.44 ± 0.50	-3.32 ± 0.50	21.28 ± 9.80	0.236 ± 0.109
103	59.28 ± 0.13	376.9	-0.21 ± 0.50	-3.09 ± 0.50	17.22 ± 7.93	0.190 ± 0.088
104	59.07 ± 0.13	377.2	-0.29 ± 0.50	-3.17 ± 0.50	18.54 ± 8.54	0.205 ± 0.096
105	58.86 ± 0.13	377.4	-0.31 ± 0.50	-3.19 ± 0.50	18.88 ± 8.69	0.209 ± 0.097
106	58.73 ± 0.13	377.6	-0.43 ± 0.50	-3.32 ± 0.50	21.28 ± 9.80	0.236 ± 0.109
107	58.48 ± 0.13	377.9	-0.22 ± 0.50	-3.11 ± 0.50	17.54 ± 8.08	0.194 ± 0.090
108	58.18 ± 0.13	378.3	-0.21 ± 0.50	-3.10 ± 0.50	17.38 ± 8.00	0.192 ± 0.089
109	58.01 ± 0.13	378.5	-0.04 ± 0.50	-2.93 ± 0.50	14.86 ± 6.84	0.164 ± 0.076
110	57.86 ± 0.13	378.7	-0.05 ± 0.50	-2.94 ± 0.50	15.00 ± 6.91	0.166 ± 0.077
111	57.67 ± 0.13	378.9	-0.36 ± 0.50	-3.25 ± 0.50	19.95 ± 9.19	0.221 ± 0.103
112	57.43 ± 0.13	379.2	-0.01 ± 0.50	-2.90 ± 0.50	14.45 ± 6.66	0.160 ± 0.074
113	57.21 ± 0.13	379.4	-0.02 ± 0.50	-2.92 ± 0.50	14.72 ± 6.78	0.163 ± 0.075
114	57.02 ± 0.13	379.7	-0.03 ± 0.50	-2.93 ± 0.50	14.86 ± 6.84	0.164 ± 0.076
115	56.81 ± 0.13	379.9	0.18 ± 0.50	-2.72 ± 0.50	12.25 ± 5.64	0.135 ± 0.062
116	56.64 ± 0.13	380.1	0.04 ± 0.50	-2.86 ± 0.50	13.93 ± 6.42	0.154 ± 0.071
117	56.35 ± 0.13	380.5	0.11 ± 0.50	-2.79 ± 0.50	13.06 ± 6.02	0.144 ± 0.067
118	56.23 ± 0.13	380.6	-0.38 ± 0.50	-3.28 ± 0.50	20.51 ± 9.45	0.226 ± 0.105
119	56.01 ± 0.13	380.9	0.03 ± 0.50	-2.87 ± 0.50	14.06 ± 6.48	0.155 ± 0.072
120	55.83 ± 0.13	381.1	0.12 ± 0.50	-2.79 ± 0.50	13.06 ± 6.02	0.144 ± 0.067
121	55.61 ± 0.13	381.4	0.08 ± 0.50	-2.83 ± 0.50	13.55 ± 6.24	0.150 ± 0.070
122	55.37 ± 0.13	381.7	0.23 ± 0.50	-2.68 ± 0.50	11.80 ± 5.44	0.131 ± 0.061
123	55.19 ± 0.13	381.9	0.21 ± 0.50	-2.70 ± 0.50	12.02 ± 5.54	0.133 ± 0.062
124	55.05 ± 0.13	382.1	0.03 ± 0.50	-2.88 ± 0.50	14.19 ± 6.54	0.157 ± 0.073
125	54.80 ± 0.13	382.4	0.14 ± 0.50	-2.77 ± 0.50	12.82 ± 5.91	0.142 ± 0.066
126	54.66 ± 0.13	382.6	0.13 ± 0.50	-2.78 ± 0.50	12.94 ± 5.96	0.143 ± 0.067

Table 4 continued on next page

Table 4 (*continued*)

N	H^a	L_D^b	$m(\text{obs})^c$	M_v^d	I^e	m_N^f
127	54.43 ± 0.13	382.9	0.02 ± 0.50	-2.90 ± 0.50	14.45 ± 6.66	0.160 ± 0.074
128	54.21 ± 0.13	383.1	0.12 ± 0.50	-2.80 ± 0.50	13.18 ± 6.07	0.146 ± 0.068
129	54.00 ± 0.13	383.4	-0.22 ± 0.50	-3.14 ± 0.50	18.03 ± 8.30	0.199 ± 0.093
130	53.85 ± 0.13	383.6	-0.12 ± 0.50	-3.04 ± 0.50	16.44 ± 7.57	0.182 ± 0.084
131	53.65 ± 0.13	383.8	0.24 ± 0.50	-2.68 ± 0.50	11.80 ± 5.44	0.131 ± 0.061
132	53.45 ± 0.13	384.1	0.53 ± 0.50	-2.39 ± 0.50	9.04 ± 4.16	0.100 ± 0.046
133	53.25 ± 0.13	384.3	0.58 ± 0.50	-2.34 ± 0.50	8.63 ± 3.97	0.095 ± 0.044
134	53.09 ± 0.13	384.5	0.29 ± 0.50	-2.63 ± 0.50	11.27 ± 5.19	0.124 ± 0.058
135	52.86 ± 0.13	384.8	0.56 ± 0.50	-2.37 ± 0.50	8.87 ± 4.09	0.098 ± 0.046
136	52.67 ± 0.13	385.1	0.65 ± 0.50	-2.28 ± 0.50	8.17 ± 3.76	0.090 ± 0.042
137	52.51 ± 0.13	385.3	0.50 ± 0.50	-2.43 ± 0.50	9.38 ± 4.32	0.104 ± 0.049
138	52.32 ± 0.13	385.5	0.59 ± 0.50	-2.34 ± 0.50	8.63 ± 3.97	0.095 ± 0.044
139	52.09 ± 0.13	385.8	0.77 ± 0.50	-2.16 ± 0.50	7.31 ± 3.37	0.080 ± 0.037
140	51.90 ± 0.13	386.0	1.01 ± 0.50	-1.92 ± 0.50	5.86 ± 2.70	0.065 ± 0.030
141	51.79 ± 0.13	386.2	1.39 ± 0.50	-1.54 ± 0.50	4.13 ± 1.90	0.046 ± 0.021
142	51.39 ± 0.13	386.7	1.10 ± 0.50	-1.84 ± 0.50	5.45 ± 2.51	0.060 ± 0.028
143	51.18 ± 0.14	386.9	1.12 ± 0.50	-1.82 ± 0.50	5.35 ± 2.46	0.059 ± 0.027
144	51.03 ± 0.14	387.1	1.39 ± 0.50	-1.55 ± 0.50	4.17 ± 1.92	0.046 ± 0.021
145	50.88 ± 0.14	387.3	1.67 ± 0.50	-1.27 ± 0.50	3.22 ± 1.48	0.036 ± 0.017
146	50.64 ± 0.14	387.6	1.56 ± 0.50	-1.38 ± 0.50	3.56 ± 1.64	0.039 ± 0.018
147	50.51 ± 0.14	387.8	1.82 ± 0.50	-1.12 ± 0.50	2.81 ± 1.29	0.031 ± 0.015
148	50.26 ± 0.14	388.1	1.54 ± 0.50	-1.40 ± 0.50	3.63 ± 1.67	0.040 ± 0.018
149	50.18 ± 0.14	388.2	1.08 ± 0.50	-1.87 ± 0.50	5.60 ± 2.58	0.062 ± 0.028
150	49.90 ± 0.14	388.5	0.97 ± 0.50	-1.98 ± 0.50	6.19 ± 2.85	0.068 ± 0.032
151	49.78 ± 0.14	388.7	0.63 ± 0.50	-2.32 ± 0.50	8.47 ± 3.90	0.094 ± 0.044
152	49.63 ± 0.14	388.9	0.55 ± 0.50	-2.40 ± 0.50	9.12 ± 4.20	0.100 ± 0.047
153	49.47 ± 0.14	389.1	0.76 ± 0.50	-2.19 ± 0.50	7.52 ± 3.46	0.083 ± 0.038
154	49.25 ± 0.14	389.4	0.88 ± 0.50	-2.07 ± 0.50	6.73 ± 3.10	0.074 ± 0.034
155	49.14 ± 0.14	389.5	1.50 ± 0.50	-1.45 ± 0.50	3.80 ± 1.75	0.042 ± 0.019
156	48.58 ± 0.14	390.2	1.68 ± 0.50	-1.28 ± 0.50	3.25 ± 1.50	0.036 ± 0.017
157	48.36 ± 0.14	390.5	1.23 ± 0.50	-1.73 ± 0.50	4.92 ± 2.27	0.055 ± 0.026
158	48.13 ± 0.14	390.8	0.56 ± 0.50	-2.40 ± 0.50	9.12 ± 4.20	0.100 ± 0.047
159	47.45 ± 0.14	391.7	2.76 ± 0.50	-0.20 ± 0.50	1.20 ± 0.55	0.014 ± 0.007

NOTE—Total mass $m=31 \pm 1$ g is the sum of m_N . Maximum brightness is $M_v=-3.93 \pm 0.50$ mag.

a Height above the sea level (km).

b Distance to meteor (km). The uncertainty on each measurement is $\lesssim 0.2$ km.

c Apparent magnitude. The uncertainty is from Equation (1).

d Absolute magnitude.

e Meteor luminosity in visual magnitude-based units.

f Mass measured on video field N (g). The duration time is 0.017 s.

Table 5. Osaka Data (ID: Osaka03_3N))

N	H^a	L_D^b	$m(\text{obs})^c$	M_v^d	I^e	m_N^f
1	87.67 ± 0.07	135.4	-0.02 ± 0.50	-0.68 ± 0.50	1.87 ± 0.86	0.021 ± 0.010
2	87.00 ± 0.07	134.2	-0.45 ± 0.50	-1.09 ± 0.50	2.73 ± 1.26	0.030 ± 0.014
3	86.88 ± 0.07	134.0	-0.42 ± 0.50	-1.06 ± 0.50	2.65 ± 1.22	0.029 ± 0.014
4	86.58 ± 0.07	133.4	0.30 ± 0.50	-0.33 ± 0.50	1.36 ± 0.62	0.015 ± 0.007
5	86.13 ± 0.07	132.6	-0.07 ± 0.50	-0.68 ± 0.50	1.87 ± 0.86	0.021 ± 0.010
6	85.94 ± 0.07	132.3	-0.40 ± 0.50	-1.01 ± 0.50	2.54 ± 1.17	0.028 ± 0.013
7	85.70 ± 0.07	131.8	-0.60 ± 0.50	-1.20 ± 0.50	3.02 ± 1.39	0.034 ± 0.016
8	85.46 ± 0.07	131.4	-1.45 ± 0.50	-2.04 ± 0.50	6.55 ± 3.01	0.072 ± 0.033
9	85.28 ± 0.07	131.1	-0.97 ± 0.50	-1.56 ± 0.50	4.21 ± 1.94	0.047 ± 0.022
10	84.97 ± 0.07	130.5	-1.07 ± 0.50	-1.65 ± 0.50	4.57 ± 2.10	0.050 ± 0.023
11	84.77 ± 0.07	130.2	-0.91 ± 0.50	-1.48 ± 0.50	3.91 ± 1.80	0.043 ± 0.020
12	84.57 ± 0.07	129.8	-1.07 ± 0.50	-1.64 ± 0.50	4.53 ± 2.09	0.050 ± 0.023
13	84.37 ± 0.07	129.5	-1.22 ± 0.50	-1.78 ± 0.50	5.15 ± 2.37	0.057 ± 0.027
14	84.11 ± 0.07	129.0	-0.64 ± 0.50	-1.19 ± 0.50	2.99 ± 1.38	0.033 ± 0.016
15	83.87 ± 0.07	128.6	-0.64 ± 0.50	-1.19 ± 0.50	2.99 ± 1.38	0.033 ± 0.016
16	83.72 ± 0.07	128.3	-0.80 ± 0.50	-1.34 ± 0.50	3.44 ± 1.58	0.038 ± 0.017
17	83.45 ± 0.07	127.8	-1.31 ± 0.50	-1.84 ± 0.50	5.45 ± 2.51	0.060 ± 0.028
18	83.32 ± 0.07	127.6	-0.88 ± 0.50	-1.41 ± 0.50	3.66 ± 1.69	0.040 ± 0.018
19	83.01 ± 0.07	127.0	-1.33 ± 0.50	-1.85 ± 0.50	5.50 ± 2.53	0.061 ± 0.028
20	82.84 ± 0.07	126.8	-1.47 ± 0.50	-1.99 ± 0.50	6.25 ± 2.88	0.069 ± 0.032
21	82.55 ± 0.07	126.2	-1.05 ± 0.50	-1.56 ± 0.50	4.21 ± 1.94	0.047 ± 0.022
22	82.48 ± 0.07	126.1	-1.89 ± 0.51	-2.39 ± 0.51	9.04 ± 4.24	0.100 ± 0.047
23	82.11 ± 0.07	125.5	-1.47 ± 0.50	-1.96 ± 0.50	6.08 ± 2.80	0.068 ± 0.031
24	81.94 ± 0.07	125.1	-1.81 ± 0.51	-2.30 ± 0.51	8.32 ± 3.91	0.092 ± 0.044
25	81.85 ± 0.07	125.0	-1.30 ± 0.50	-1.78 ± 0.50	5.15 ± 2.37	0.057 ± 0.027
26	81.45 ± 0.07	124.3	-1.78 ± 0.51	-2.25 ± 0.51	7.94 ± 3.73	0.088 ± 0.041
27	81.19 ± 0.06	123.8	-1.84 ± 0.51	-2.30 ± 0.51	8.32 ± 3.91	0.092 ± 0.044
28	80.91 ± 0.06	123.3	-1.19 ± 0.50	-1.64 ± 0.50	4.53 ± 2.09	0.050 ± 0.023
29	80.78 ± 0.06	123.1	-1.71 ± 0.51	-2.16 ± 0.51	7.31 ± 3.43	0.080 ± 0.037
30	80.48 ± 0.06	122.6	-1.07 ± 0.50	-1.51 ± 0.50	4.02 ± 1.85	0.045 ± 0.021
31	80.28 ± 0.06	122.2	-2.09 ± 0.52	-2.53 ± 0.52	10.28 ± 4.92	0.113 ± 0.055
32	80.10 ± 0.06	121.9	-1.78 ± 0.51	-2.21 ± 0.51	7.66 ± 3.60	0.085 ± 0.040
33	79.80 ± 0.06	121.4	-1.55 ± 0.51	-1.97 ± 0.51	6.14 ± 2.88	0.068 ± 0.032
34	79.59 ± 0.06	121.0	-2.08 ± 0.52	-2.49 ± 0.52	9.91 ± 4.75	0.110 ± 0.053
35	79.32 ± 0.06	120.5	-1.61 ± 0.51	-2.01 ± 0.51	6.37 ± 2.99	0.070 ± 0.033
36	79.14 ± 0.06	120.2	-1.66 ± 0.51	-2.06 ± 0.51	6.67 ± 3.13	0.074 ± 0.035
37	78.87 ± 0.06	119.7	-1.56 ± 0.51	-1.95 ± 0.51	6.03 ± 2.83	0.067 ± 0.031
38	78.72 ± 0.06	119.5	-1.87 ± 0.51	-2.26 ± 0.51	8.02 ± 3.77	0.089 ± 0.042
39	78.47 ± 0.06	119.0	-1.90 ± 0.51	-2.28 ± 0.51	8.17 ± 3.84	0.090 ± 0.043
40	78.19 ± 0.06	118.5	-1.41 ± 0.50	-1.78 ± 0.50	5.15 ± 2.37	0.057 ± 0.027

Table 5 continued on next page

Table 5 (*continued*)

N	H^a	L_D^b	$m(\text{obs})^c$	M_v^d	I^e	m_N^f
41	78.01 ± 0.06	118.2	-1.90 ± 0.51	-2.26 ± 0.51	8.02 ± 3.77	0.089 ± 0.042
42	77.76 ± 0.06	117.8	-1.56 ± 0.51	-1.92 ± 0.51	5.86 ± 2.75	0.065 ± 0.030
43	77.51 ± 0.06	117.4	-1.54 ± 0.51	-1.89 ± 0.51	5.70 ± 2.68	0.063 ± 0.030
44	77.38 ± 0.06	117.1	-1.87 ± 0.51	-2.21 ± 0.51	7.66 ± 3.60	0.085 ± 0.040
45	77.15 ± 0.06	116.7	-2.11 ± 0.52	-2.45 ± 0.52	9.55 ± 4.57	0.106 ± 0.051
46	76.83 ± 0.06	116.2	-2.20 ± 0.52	-2.53 ± 0.52	10.28 ± 4.92	0.113 ± 0.055
47	76.70 ± 0.06	115.9	-2.32 ± 0.53	-2.64 ± 0.53	11.38 ± 5.55	0.126 ± 0.062
48	76.41 ± 0.06	115.4	-1.88 ± 0.51	-2.19 ± 0.51	7.52 ± 3.53	0.083 ± 0.039
49	76.18 ± 0.06	115.0	-2.21 ± 0.52	-2.51 ± 0.52	10.09 ± 4.83	0.111 ± 0.054
50	76.00 ± 0.06	114.7	-2.00 ± 0.51	-2.30 ± 0.51	8.32 ± 3.91	0.092 ± 0.044
51	75.72 ± 0.06	114.3	-1.98 ± 0.51	-2.27 ± 0.51	8.09 ± 3.80	0.090 ± 0.042
52	75.52 ± 0.06	113.9	-2.17 ± 0.52	-2.45 ± 0.52	9.55 ± 4.57	0.106 ± 0.051
53	75.23 ± 0.06	113.4	-2.26 ± 0.52	-2.53 ± 0.52	10.28 ± 4.92	0.113 ± 0.055
54	75.03 ± 0.06	113.1	-2.78 ± 0.55	-3.05 ± 0.55	16.60 ± 8.41	0.184 ± 0.094
55	74.84 ± 0.06	112.7	-2.89 ± 0.56	-3.15 ± 0.56	18.20 ± 9.39	0.201 ± 0.104
56	74.46 ± 0.06	112.1	-3.16 ± 0.58	-3.41 ± 0.58	23.12 ± 12.35	0.256 ± 0.138
57	74.24 ± 0.06	111.7	-3.22 ± 0.59	-3.46 ± 0.59	24.21 ± 13.16	0.268 ± 0.147
58	73.85 ± 0.06	111.0	-3.15 ± 0.58	-3.38 ± 0.58	22.49 ± 12.01	0.249 ± 0.134
59	73.70 ± 0.06	110.8	-3.59 ± 0.63	-3.81 ± 0.63	33.42 ± 19.39	0.370 ± 0.216
60	73.41 ± 0.06	110.3	-3.41 ± 0.61	-3.62 ± 0.61	28.05 ± 15.76	0.311 ± 0.176
61	73.07 ± 0.06	109.7	-2.98 ± 0.57	-3.18 ± 0.57	18.71 ± 9.82	0.207 ± 0.110
62	72.85 ± 0.06	109.3	-2.70 ± 0.55	-2.89 ± 0.55	14.32 ± 7.26	0.158 ± 0.081
63	72.59 ± 0.06	108.8	-2.81 ± 0.55	-2.99 ± 0.55	15.70 ± 7.95	0.174 ± 0.089
64	72.60 ± 0.06	108.9	-3.21 ± 0.59	-3.40 ± 0.59	22.91 ± 12.45	0.253 ± 0.138
65	72.29 ± 0.06	108.3	-2.84 ± 0.56	-3.01 ± 0.56	16.00 ± 8.25	0.177 ± 0.092
66	72.04 ± 0.06	107.9	-3.13 ± 0.58	-3.30 ± 0.58	20.89 ± 11.16	0.231 ± 0.125
67	71.85 ± 0.06	107.6	-2.93 ± 0.56	-3.09 ± 0.56	17.22 ± 8.88	0.190 ± 0.099
68	71.54 ± 0.06	107.1	-2.33 ± 0.53	-2.48 ± 0.53	9.82 ± 4.79	0.109 ± 0.053
69	71.50 ± 0.06	107.0	-2.79 ± 0.55	-2.94 ± 0.55	15.00 ± 7.60	0.166 ± 0.085
70	71.17 ± 0.06	106.4	-2.94 ± 0.56	-3.07 ± 0.56	16.90 ± 8.72	0.187 ± 0.097
71	71.03 ± 0.06	106.2	-2.81 ± 0.55	-2.94 ± 0.55	15.00 ± 7.60	0.166 ± 0.085
72	70.82 ± 0.06	105.8	-2.77 ± 0.55	-2.89 ± 0.55	14.32 ± 7.26	0.158 ± 0.081
73	70.58 ± 0.06	105.4	-2.92 ± 0.56	-3.03 ± 0.56	16.29 ± 8.40	0.180 ± 0.094
74	70.33 ± 0.05	105.0	-2.89 ± 0.56	-3.00 ± 0.56	15.85 ± 8.17	0.175 ± 0.091
75	70.24 ± 0.05	104.9	-3.01 ± 0.57	-3.11 ± 0.57	17.54 ± 9.21	0.194 ± 0.103
76	69.91 ± 0.05	104.3	-3.17 ± 0.58	-3.26 ± 0.58	20.14 ± 10.76	0.223 ± 0.120
77	69.66 ± 0.05	103.9	-3.05 ± 0.57	-3.13 ± 0.57	17.86 ± 9.38	0.197 ± 0.104
78	69.47 ± 0.05	103.6	-3.24 ± 0.59	-3.32 ± 0.59	21.28 ± 11.56	0.236 ± 0.129
79	69.25 ± 0.05	103.2	-3.33 ± 0.60	-3.40 ± 0.60	22.91 ± 12.66	0.253 ± 0.141
80	68.99 ± 0.05	102.7	-3.26 ± 0.59	-3.32 ± 0.59	21.28 ± 11.56	0.236 ± 0.129
81	68.75 ± 0.05	102.3	-3.29 ± 0.60	-3.34 ± 0.60	21.68 ± 11.98	0.239 ± 0.133
82	68.53 ± 0.05	102.0	-3.29 ± 0.60	-3.33 ± 0.60	21.48 ± 11.87	0.238 ± 0.132
83	68.18 ± 0.05	101.4	-3.23 ± 0.59	-3.26 ± 0.59	20.14 ± 10.94	0.223 ± 0.122

Table 5 continued on next page

Table 5 (*continued*)

N	<i>H</i> ^a	<i>L_D</i> ^b	<i>m</i> (obs) ^c	<i>M_v</i> ^d	<i>I</i> ^e	<i>m_N</i> ^f
84	68.13 ± 0.05	101.3	-3.26 ± 0.59	-3.29 ± 0.59	20.70 ± 11.25	0.229 ± 0.125
85	67.86 ± 0.05	100.9	-3.50 ± 0.62	-3.52 ± 0.62	25.59 ± 14.61	0.283 ± 0.162
86	67.66 ± 0.05	100.5	-3.61 ± 0.63	-3.62 ± 0.63	28.05 ± 16.28	0.311 ± 0.182
87	67.34 ± 0.05	100.0	-4.24 ± 0.74	-4.24 ± 0.74	49.66 ± 33.85	0.549 ± 0.375
88	67.14 ± 0.05	99.7	-4.55 ± 0.80	-4.54 ± 0.80	65.46 ± 48.24	0.724 ± 0.536
89	66.69 ± 0.05	98.9	-4.10 ± 0.71	-4.08 ± 0.71	42.85 ± 28.02	0.474 ± 0.311
90	66.51 ± 0.05	98.6	-3.02 ± 0.57	-2.99 ± 0.57	15.70 ± 8.24	0.174 ± 0.092
91	65.98 ± 0.05	97.8	-2.14 ± 0.52	-2.09 ± 0.52	6.85 ± 3.28	0.076 ± 0.037
92	65.86 ± 0.05	97.5	-1.54 ± 0.51	-1.49 ± 0.51	3.94 ± 1.85	0.044 ± 0.021
93	65.68 ± 0.05	97.2	-1.34 ± 0.50	-1.28 ± 0.50	3.25 ± 1.50	0.036 ± 0.017
94	65.81 ± 0.05	97.5	-2.81 ± 0.55	-2.76 ± 0.55	12.71 ± 6.44	0.141 ± 0.072
95	65.67 ± 0.05	97.2	-3.42 ± 0.61	-3.36 ± 0.61	22.08 ± 12.41	0.244 ± 0.137
96	65.48 ± 0.05	96.9	-3.61 ± 0.63	-3.54 ± 0.63	26.06 ± 15.12	0.288 ± 0.168
97	65.19 ± 0.05	96.4	-3.28 ± 0.60	-3.20 ± 0.60	19.05 ± 10.53	0.211 ± 0.117
98	64.95 ± 0.05	96.1	-3.16 ± 0.58	-3.07 ± 0.58	16.90 ± 9.03	0.187 ± 0.101
99	64.67 ± 0.05	95.6	-3.62 ± 0.64	-3.52 ± 0.64	25.59 ± 15.08	0.283 ± 0.167
100	64.54 ± 0.05	95.4	-3.52 ± 0.62	-3.42 ± 0.62	23.33 ± 13.33	0.258 ± 0.149
101	64.22 ± 0.05	94.9	-3.06 ± 0.57	-2.95 ± 0.57	15.14 ± 7.95	0.167 ± 0.088
102	64.09 ± 0.05	94.6	-2.11 ± 0.52	-1.99 ± 0.52	6.25 ± 2.99	0.069 ± 0.033
103	63.92 ± 0.05	94.4	-3.00 ± 0.57	-2.87 ± 0.57	14.06 ± 7.38	0.155 ± 0.082
104	63.72 ± 0.05	94.1	-3.22 ± 0.59	-3.09 ± 0.59	17.22 ± 9.36	0.190 ± 0.104
105	63.48 ± 0.05	93.7	-3.27 ± 0.59	-3.13 ± 0.59	17.86 ± 9.71	0.197 ± 0.108
106	63.32 ± 0.05	93.4	-3.37 ± 0.61	-3.22 ± 0.61	19.41 ± 10.90	0.215 ± 0.121
107	63.08 ± 0.05	93.0	-3.53 ± 0.62	-3.37 ± 0.62	22.28 ± 12.73	0.247 ± 0.142
108	62.87 ± 0.05	92.7	-2.95 ± 0.56	-2.79 ± 0.56	13.06 ± 6.74	0.144 ± 0.075
109	62.66 ± 0.05	92.3	-2.85 ± 0.56	-2.68 ± 0.56	11.80 ± 6.09	0.131 ± 0.068
110	62.48 ± 0.05	92.0	-3.28 ± 0.60	-3.10 ± 0.60	17.38 ± 9.60	0.192 ± 0.106
111	62.23 ± 0.05	91.6	-3.53 ± 0.62	-3.34 ± 0.62	21.68 ± 12.38	0.239 ± 0.137
112	61.96 ± 0.05	91.2	-4.04 ± 0.70	-3.84 ± 0.70	34.36 ± 22.15	0.380 ± 0.246
113	61.75 ± 0.05	90.9	-3.26 ± 0.59	-3.05 ± 0.59	16.60 ± 9.02	0.184 ± 0.101
114	61.60 ± 0.05	90.6	-2.89 ± 0.56	-2.68 ± 0.56	11.80 ± 6.09	0.131 ± 0.068
115	61.41 ± 0.05	90.3	-3.01 ± 0.57	-2.79 ± 0.57	13.06 ± 6.86	0.144 ± 0.076
116	61.16 ± 0.05	89.9	-3.42 ± 0.61	-3.19 ± 0.61	18.88 ± 10.61	0.209 ± 0.118
117	61.04 ± 0.05	89.8	-3.23 ± 0.59	-3.00 ± 0.59	15.85 ± 8.61	0.175 ± 0.096
118	60.84 ± 0.05	89.4	-2.79 ± 0.55	-2.55 ± 0.55	10.47 ± 5.30	0.116 ± 0.060
119	60.55 ± 0.05	89.0	-2.97 ± 0.57	-2.72 ± 0.57	12.25 ± 6.43	0.135 ± 0.071
120	60.41 ± 0.05	88.8	-3.23 ± 0.59	-2.97 ± 0.59	15.42 ± 8.38	0.171 ± 0.094
121	60.24 ± 0.05	88.5	-3.38 ± 0.61	-3.11 ± 0.61	17.54 ± 9.85	0.194 ± 0.109
122	60.07 ± 0.05	88.2	-3.19 ± 0.59	-2.92 ± 0.59	14.72 ± 8.00	0.163 ± 0.089
123	59.74 ± 0.05	87.7	-2.90 ± 0.56	-2.61 ± 0.56	11.07 ± 5.71	0.122 ± 0.063
124	59.62 ± 0.05	87.5	-3.11 ± 0.58	-2.82 ± 0.58	13.43 ± 7.17	0.149 ± 0.080
125	59.39 ± 0.05	87.2	-3.47 ± 0.62	-3.17 ± 0.62	18.54 ± 10.58	0.205 ± 0.117
126	59.25 ± 0.05	87.0	-3.30 ± 0.60	-3.00 ± 0.60	15.85 ± 8.76	0.175 ± 0.097

Table 5 continued on next page

Table 5 (*continued*)

N	<i>H</i> ^a	<i>L</i> _D ^b	<i>m</i> (obs) ^c	<i>M</i> _v ^d	<i>I</i> ^e	<i>m</i> _N ^f
127	59.04 ± 0.05	86.6	-3.08 ± 0.58	-2.77 ± 0.58	12.82 ± 6.85	0.142 ± 0.076
128	58.96 ± 0.05	86.5	-3.09 ± 0.58	-2.78 ± 0.58	12.94 ± 6.91	0.143 ± 0.077
129	58.59 ± 0.04	85.9	-3.21 ± 0.59	-2.88 ± 0.59	14.19 ± 7.71	0.157 ± 0.086
130	58.46 ± 0.04	85.7	-3.23 ± 0.59	-2.89 ± 0.59	14.32 ± 7.78	0.158 ± 0.086
131	58.20 ± 0.04	85.3	-2.97 ± 0.57	-2.62 ± 0.57	11.17 ± 5.86	0.123 ± 0.065
132	58.00 ± 0.04	85.0	-3.06 ± 0.57	-2.71 ± 0.57	12.13 ± 6.37	0.134 ± 0.070
133	57.78 ± 0.04	84.7	-3.65 ± 0.64	-3.29 ± 0.64	20.70 ± 12.20	0.229 ± 0.135
134	57.63 ± 0.04	84.5	-3.53 ± 0.62	-3.16 ± 0.62	18.37 ± 10.49	0.203 ± 0.116
135	57.37 ± 0.04	84.1	-3.19 ± 0.59	-2.81 ± 0.59	13.30 ± 7.23	0.147 ± 0.081
136	57.25 ± 0.04	83.9	-3.17 ± 0.58	-2.79 ± 0.58	13.06 ± 6.98	0.144 ± 0.078
137	56.97 ± 0.04	83.4	-3.00 ± 0.57	-2.61 ± 0.57	11.07 ± 5.81	0.122 ± 0.065
138	56.83 ± 0.04	83.2	-3.35 ± 0.60	-2.95 ± 0.60	15.14 ± 8.36	0.167 ± 0.092
139	56.69 ± 0.04	83.0	-3.37 ± 0.61	-2.97 ± 0.61	15.42 ± 8.66	0.171 ± 0.096
140	56.40 ± 0.04	82.6	-3.36 ± 0.60	-2.94 ± 0.60	15.00 ± 8.29	0.166 ± 0.092
141	56.29 ± 0.04	82.4	-3.17 ± 0.58	-2.75 ± 0.58	12.59 ± 6.73	0.139 ± 0.075
142	56.04 ± 0.04	82.1	-3.21 ± 0.59	-2.78 ± 0.59	12.94 ± 7.03	0.143 ± 0.079
143	55.85 ± 0.04	81.8	-3.12 ± 0.58	-2.68 ± 0.58	11.80 ± 6.31	0.131 ± 0.071
144	55.66 ± 0.04	81.5	-4.07 ± 0.70	-3.63 ± 0.70	28.31 ± 18.25	0.313 ± 0.203
145	55.40 ± 0.04	81.1	-3.65 ± 0.64	-3.20 ± 0.64	19.05 ± 11.23	0.211 ± 0.125
146	55.08 ± 0.04	80.6	-2.16 ± 0.52	-1.69 ± 0.52	4.74 ± 2.27	0.052 ± 0.025
147	55.04 ± 0.04	80.6	-2.98 ± 0.57	-2.51 ± 0.57	10.09 ± 5.30	0.111 ± 0.058
148	54.88 ± 0.04	80.3	-3.10 ± 0.58	-2.62 ± 0.58	11.17 ± 5.97	0.123 ± 0.066
149	54.69 ± 0.04	80.1	-3.27 ± 0.59	-2.79 ± 0.59	13.06 ± 7.10	0.144 ± 0.079
150	54.53 ± 0.04	79.8	-3.22 ± 0.59	-2.73 ± 0.59	12.36 ± 6.72	0.137 ± 0.075
151	54.29 ± 0.04	79.5	-3.12 ± 0.58	-2.62 ± 0.58	11.17 ± 5.97	0.123 ± 0.066
152	54.19 ± 0.04	79.3	-3.16 ± 0.58	-2.66 ± 0.58	11.59 ± 6.19	0.128 ± 0.069
153	53.94 ± 0.04	79.0	-2.98 ± 0.57	-2.47 ± 0.57	9.73 ± 5.11	0.108 ± 0.057
154	53.79 ± 0.04	78.7	-2.94 ± 0.56	-2.42 ± 0.56	9.29 ± 4.79	0.102 ± 0.053
155	53.61 ± 0.04	78.5	-2.96 ± 0.56	-2.43 ± 0.56	9.38 ± 4.84	0.104 ± 0.054
156	53.41 ± 0.04	78.2	-2.71 ± 0.55	-2.18 ± 0.55	7.45 ± 3.77	0.082 ± 0.042
157	53.29 ± 0.04	78.0	-2.86 ± 0.56	-2.32 ± 0.56	8.47 ± 4.37	0.094 ± 0.049
158	53.08 ± 0.04	77.7	-2.68 ± 0.54	-2.13 ± 0.54	7.11 ± 3.54	0.079 ± 0.040
159	52.97 ± 0.04	77.6	-2.99 ± 0.57	-2.44 ± 0.57	9.46 ± 4.97	0.105 ± 0.056
160	52.78 ± 0.04	77.3	-3.06 ± 0.57	-2.50 ± 0.57	10.00 ± 5.25	0.111 ± 0.059
161	52.57 ± 0.04	77.0	-2.60 ± 0.54	-2.03 ± 0.54	6.49 ± 3.23	0.072 ± 0.036
162	52.51 ± 0.04	76.9	-2.52 ± 0.54	-1.95 ± 0.54	6.03 ± 3.00	0.067 ± 0.033
163	52.24 ± 0.04	76.5	-2.71 ± 0.55	-2.13 ± 0.55	7.11 ± 3.60	0.079 ± 0.041
164	52.03 ± 0.04	76.2	-2.52 ± 0.54	-1.93 ± 0.54	5.92 ± 2.94	0.066 ± 0.033
165	51.82 ± 0.04	75.9	-2.86 ± 0.56	-2.26 ± 0.56	8.02 ± 4.13	0.089 ± 0.046
166	51.65 ± 0.04	75.7	-3.28 ± 0.60	-2.68 ± 0.60	11.80 ± 6.52	0.131 ± 0.073
167	51.41 ± 0.04	75.4	-3.58 ± 0.63	-2.97 ± 0.63	15.42 ± 8.95	0.171 ± 0.100
168	51.20 ± 0.04	75.1	-3.43 ± 0.61	-2.81 ± 0.61	13.30 ± 7.47	0.147 ± 0.083
169	51.05 ± 0.04	74.9	-3.02 ± 0.57	-2.39 ± 0.57	9.04 ± 4.74	0.100 ± 0.052

Table 5 continued on next page

Table 5 (*continued*)

N	<i>H</i> ^a	<i>L_D</i> ^b	<i>m</i> (obs) ^c	<i>M_v</i> ^d	<i>I</i> ^e	<i>m_N</i> ^f
170	50.91 ± 0.04	74.7	-2.89 ± 0.56	-2.26 ± 0.56	8.02 ± 4.13	0.089 ± 0.046
171	50.85 ± 0.04	74.6	-2.88 ± 0.56	-2.24 ± 0.56	7.87 ± 4.06	0.087 ± 0.045
172	50.64 ± 0.04	74.3	-2.67 ± 0.54	-2.02 ± 0.54	6.43 ± 3.20	0.071 ± 0.036
173	50.47 ± 0.04	74.1	-2.62 ± 0.54	-1.97 ± 0.54	6.14 ± 3.05	0.068 ± 0.034
174	50.38 ± 0.04	74.0	-2.08 ± 0.52	-1.43 ± 0.52	3.73 ± 1.79	0.041 ± 0.020
175	50.15 ± 0.04	73.6	-3.14 ± 0.58	-2.47 ± 0.58	9.73 ± 5.20	0.108 ± 0.058
176	50.06 ± 0.04	73.5	-3.14 ± 0.58	-2.47 ± 0.58	9.73 ± 5.20	0.108 ± 0.058
177	49.87 ± 0.04	73.3	-3.31 ± 0.60	-2.64 ± 0.60	11.38 ± 6.29	0.126 ± 0.070
178	49.80 ± 0.04	73.2	-2.41 ± 0.53	-1.73 ± 0.53	4.92 ± 2.40	0.055 ± 0.027
179	49.61 ± 0.04	72.9	-1.67 ± 0.51	-0.98 ± 0.51	2.47 ± 1.16	0.027 ± 0.013
180	49.48 ± 0.04	72.7	-2.24 ± 0.52	-1.55 ± 0.52	4.17 ± 2.00	0.046 ± 0.022
181	49.37 ± 0.04	72.6	-2.12 ± 0.52	-1.42 ± 0.52	3.70 ± 1.77	0.041 ± 0.020
182	49.29 ± 0.04	72.5	-2.08 ± 0.52	-1.38 ± 0.52	3.56 ± 1.71	0.039 ± 0.019
183	49.12 ± 0.04	72.3	-2.07 ± 0.52	-1.37 ± 0.52	3.53 ± 1.69	0.039 ± 0.019
184	49.04 ± 0.04	72.2	-1.97 ± 0.51	-1.26 ± 0.51	3.19 ± 1.50	0.036 ± 0.017
185	48.91 ± 0.04	72.0	-1.80 ± 0.51	-1.09 ± 0.51	2.73 ± 1.28	0.030 ± 0.015
186	48.75 ± 0.04	71.8	-1.24 ± 0.50	-0.52 ± 0.50	1.61 ± 0.74	0.017 ± 0.008
187	48.63 ± 0.04	71.6	-1.52 ± 0.50	-0.79 ± 0.50	2.07 ± 0.95	0.023 ± 0.011
188	48.51 ± 0.04	71.5	-1.85 ± 0.51	-1.12 ± 0.51	2.81 ± 1.32	0.031 ± 0.015
189	48.38 ± 0.04	71.3	-0.88 ± 0.50	-0.15 ± 0.50	1.15 ± 0.53	0.013 ± 0.006
190	48.26 ± 0.04	71.1	-1.64 ± 0.51	-0.90 ± 0.51	2.29 ± 1.08	0.026 ± 0.012
191	48.13 ± 0.04	71.0	-1.44 ± 0.50	-0.70 ± 0.50	1.91 ± 0.88	0.021 ± 0.010
192	48.03 ± 0.04	70.8	-1.10 ± 0.50	-0.35 ± 0.50	1.38 ± 0.64	0.016 ± 0.008
193	47.88 ± 0.04	70.6	0.11 ± 0.50	0.87 ± 0.50	0.45 ± 0.21	0.005 ± 0.002
194	47.79 ± 0.04	70.5	0.49 ± 0.50	1.25 ± 0.50	0.32 ± 0.15	0.004 ± 0.002

NOTE—Total mass $m=26 \pm 1$ g is the sum of m_N . Maximum brightness is $M_v=-4.54 \pm 0.80$ mag.^aHeight above the sea level (km).^bDistance to meteor (km). The uncertainty on each measurement is $\lesssim 0.2$ km.^cApparent magnitude. The uncertainty is from Equation (1).^dAbsolute magnitude.^eMeteor luminosity in visual magnitude-based units.^fMass measured on video field N (g). The duration time is 0.017 s.

Table 6. *D*-criterions

Criterion	Value	Source
D_{SH}	0.0079	(1)
D'	0.0091	(2)
D_{ACS}	0.0061	(3)

References—

- (1) Southworth & Hawkins
(1963)
- (2) Drummond (1981)
- (3) Asher et al. (1993)

Table 7. Mass Comparison

Data	Classical Model ^a	New Model ^b
Tokyo	11±1 g	31±1 g
Osaka	9±1 g	26±1 g
-	10±1 g ^c	29±1 g ^c

^aEquation (B2) (e.g. Cephecha et al. 1998).

^bEquation (B9) from this work.

^cThe weighted mean of measurements.

Table 8. Meteor Search in SonotaCo Network and EDMOND Databases

Data No.	UT ^a	λ_s ^b (deg)	α ^c (deg)	δ ^d (deg)	v_g ^e (km s ⁻¹)	a ^f (AU)	e ^g	i ^h (deg)	q ⁱ (AU)	ω ^j (deg)	Ω ^k (deg)
Descending Node											
SonotaCo											
1	2010 Apr 16 18:08:41	26.5027	305.10	36.25	33.6	1.079	0.296	66.8	0.759	86.2	26.503
2	2011 May 08 15:25:36	47.5478	307.11	39.91	17.5	0.774	0.312	36.1	0.533	9.9	47.548
3	2013 Apr 22 18:45:38	32.6091	331.27	44.57	19.2	0.957	0.355	33.5	0.617	61.7	32.609
4	2013 May 13 16:58:56	52.9028	303.43	63.69	23.8	1.544	0.364	42.7	0.982	153.3	52.903
5	2015 May 09 18:45:44	48.6164	309.12	60.33	25.2	1.467	0.347	45.5	0.957	143.0	48.616
EDMOND											
6	2007 Apr 28 00:21:33	37.2620	337.63	43.36	26.1	1.110	0.481	44.9	0.576	71.6	37.262
7	2008 Apr 14 22:01:17	25.2108	305.02	38.83	29.0	0.998	0.272	57.5	0.726	73.1	25.211
8	2008 May 07 00:33:43	46.7232	339.21	44.20	27.2	1.020	0.463	49.8	0.548	63.6	46.723
9	2009 Apr 11 23:19:58	22.0683	322.24	46.81	17.3	1.008	0.287	30.3	0.719	74.5	22.069
10	2009 Apr 22 00:20:56	31.8898	301.19	45.25	31.6	1.317	0.291	59.9	0.934	133.2	31.890
11	2009 May 11 23:44:06	51.2722	305.20	52.71	29.1	1.360	0.278	54.8	0.982	150.6	51.272
12	2010 Apr 08 22:38:54	18.8401	339.18	53.61	17.2	1.381	0.401	26.2	0.827	113.0	18.840
13	2011 Apr 23 20:30:16	33.1847	314.67	42.29	27.8	1.019	0.312	54.0	0.701	74.2	33.185
14	2011 May 03 22:57:34	43.0077	337.37	49.87	25.8	1.194	0.432	45.2	0.678	85.1	43.008
15	2011 May 06 20:32:49	45.8181	302.83	55.76	24.5	1.255	0.227	46.0	0.970	142.4	45.818
16	2011 May 09 00:37:59	47.9189	308.65	47.90	32.7	1.355	0.295	62.2	0.956	140.0	47.919
17	2012 Apr 26 02:49:16	36.1120	312.80	41.43	34.7	1.284	0.364	66.6	0.817	107.2	36.112
18	2014 Apr 24 00:56:19	33.5844	302.11	41.38	21.0	0.846	0.234	42.9	0.648	28.7	33.584
19	2015 Apr 24 03:20:15	33.4362	325.77	47.71	22.8	1.065	0.344	41.1	0.699	79.0	33.436
20	2016 Apr 30 21:09:05	40.7152	321.69	46.50	31.1	1.267	0.392	58.1	0.771	99.5	40.715
Ascending Node											
SonotaCo											
21	2008 Oct 20 18:57:59	207.6334	73.36	-33.07	22.8	1.065	0.357	40.5	0.685	100.7	27.634
22	2011 Oct 26 16:20:31	212.7369	76.86	-34.25	22.2	1.076	0.336	39.4	0.715	96.8	32.737

NOTE—From SonotaCo Network Data Sets^a in 2007–2018 and EDMOND Database^b in 2001–2016.

^aObserved Date and Time.

^bSolar longitude (J2000.0).

^cRight ascension (J2000.0).

^dDeclination (J2000.0).

^eGeocentric velocity.

^fSemimajor axis.

^gEccentricity.

^hInclination.

ⁱPerihelion distance.

^jArgument of perihelion.

^kLongitude of ascending node.

^a<http://sonotaco.jp/doc/SNM/index.html>

^b<https://www.meteornews.net/edmond/edmond-database/>

Table 9. D-criterions for Searched Meteors

Data No.	2003 YT ₁			Fireball		
	D_{SH}^a	D'^b	D_{ACS}^c	D_{SH}^a	D'^b	D_{ACS}^c
Descending Node						
SonotaCo						
1	0.436	0.177	0.394	0.439	0.178	0.397
2	0.469	0.260	0.180	0.468	0.257	0.177
3	0.329	0.243	0.202	0.325	0.239	0.197
4	0.491	0.212	0.163	0.494	0.210	0.160
5	0.397	0.173	0.133	0.401	0.171	0.132
EDMOND						
6	0.315	0.348	0.190	0.310	0.342	0.185
7	0.334	0.159	0.237	0.337	0.162	0.241
8	0.350	0.346	0.200	0.346	0.340	0.198
9	0.342	0.191	0.243	0.340	0.192	0.239
10	0.370	0.142	0.283	0.375	0.145	0.287
11	0.465	0.177	0.205	0.470	0.181	0.208
12	0.382	0.201	0.342	0.378	0.195	0.337
13	0.235	0.162	0.176	0.236	0.161	0.179
14	0.187	0.277	0.144	0.181	0.271	0.140
15	0.336	0.185	0.088	0.341	0.193	0.092
16	0.477	0.174	0.325	0.482	0.177	0.328
17	0.407	0.175	0.401	0.410	0.171	0.403
18	0.332	0.195	0.107	0.334	0.199	0.110
19	0.158	0.195	0.075	0.154	0.192	0.070
20	0.274	0.169	0.269	0.275	0.163	0.270
Ascending Node						
SonotaCo						
21	0.185	0.130	0.092	0.179	0.121	0.086
22	0.134	0.091	0.094	0.127	0.083	0.088

NOTE—Significance is set to $D < 0.20$ (Williams et al. 2019).

^aSouthworth & Hawkins (1963)

^bDrummond (1981)

^cAsher et al. (1993)

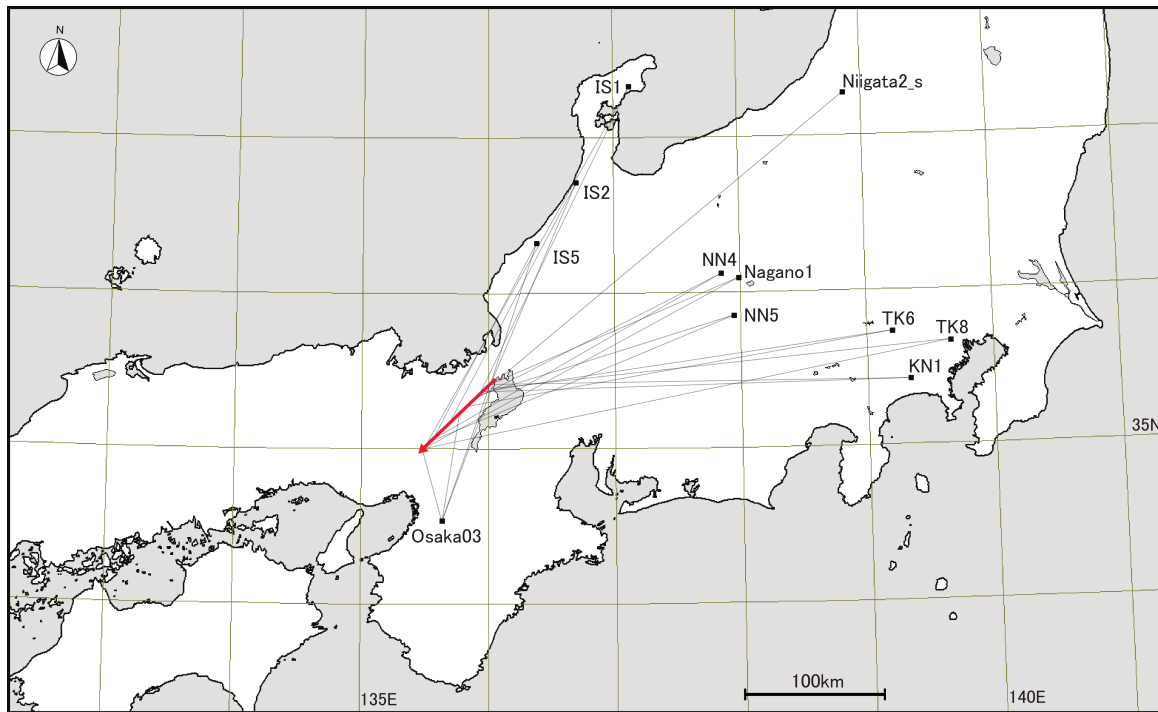


Figure 1. Map showing the projection of fireball atmospheric trajectory (red arrow), including eleven observation sites (ID) and the lines of sight (thin-line). The direct distance of trajectory is approximately 70 km. The ID is listed in <http://sonotaco.jp/doc/SNM/2017C.txt>. ©SonotaCo.



(a) Composite image, with 204 fields (3.40 sec): Watec (WAT-231S2), $f=3$ mm, F0.95 and FOV= $94^\circ \times 68^\circ$ at Osaka (Osaka03_3N).



(b) The 173 fields (2.89 sec): Watec (WAT-100N), $f=8$ mm, F0.8 and FOV= $45^\circ \times 34^\circ$ at Tokyo (TK8_S7).



(c) The 164 fields (2.74 sec): Watec, $f=6$ mm, F1.2 and FOV= $57^\circ \times 43^\circ$ at Ishikawa (IS5_SW).



(d) The 162 fields (2.70 sec): Watec (WAT-100N), $f=3.8$ mm, F0.8 and FOV= $89^\circ \times 69^\circ$ at Ishikawa (IS1).



(e) The 104 fields (1.74 sec): Sony α7s (High-definition 1920×1080 pixel, 60i, interlaced), $f=8$ mm, F3.5 and fish-eye lens at Nagano (NN4_FE).



(f) The 41 fields (0.68 sec): Watec (WAT-100N), $f=6$ mm, F0.8 and FOV= $57^\circ \times 43^\circ$ at Tokyo (TK6_w).

Figure 2. Composite images of the fireball recorded on UT 2017 April 28 at 15^h 58^m 19^s. Number of detected video fields (duration time): camera, focal length (f), F-number and FOV at observation site (ID). The date and time within image is JST.

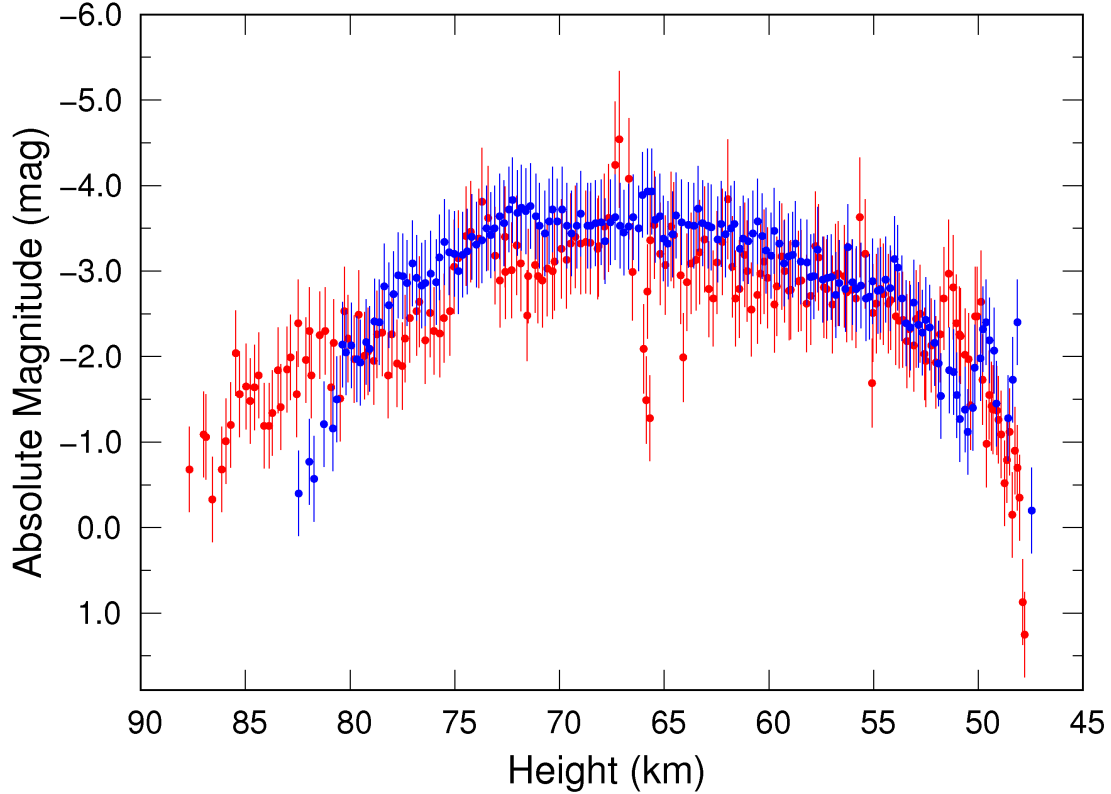


Figure 3. Light curves of fireball measured at Tokyo (Blue) and Osaka (Red). Absolute magnitudes as a function of height are plotted from Tables 4 and 5. The weighted mean of maximum brightness is -4.10 ± 0.42 mag. The uncertainty of height is within the circle.